Multiplexing Techniques and Design-Automation Tools for FRET-Enabled Optical Computing

by

Mohammad Mottaghi Dastjerdi

Department of Computer Science
Duke University

Date:_____

Approved:

_____
Christopher L. Dwyer, Supervisor

_____
Alvin R. Lebeck

_____
Daniel Sorin

_____
Benjamin C. Lee

Dissertation submitted in partial fulfillment of
the requirements for the degree of
Doctor of Philosophy in the Department of
Computer Science in the Graduate School of
Duke University

2014

ABSTRACT

Multiplexing Techniques and Design-Automation Tools for FRET-Enabled Optical Computing

by

Mohammad Mottaghi Dastjerdi

Department of Computer Science
Duke University

Date:_____

Approved:

_____
Christopher L. Dwyer, Supervisor

_____
Alvin R. Lebeck

_____
Daniel Sorin

_____
Benjamin C. Lee

An abstract of a dissertation submitted in partial fulfillment of the requirements for the degree of Doctor of Philosophy in the Department of Computer Science in the Graduate School of Duke University

2014

Abstract

FRET-enabled optical computing is a new computing paradigm that uses the energy of incident photons to perform computation in molecular-scale circuits composed of inter-communicating photoactive molecules. Unlike conventional computing approaches, computation in these circuits does not require any electric current; instead, it relies on the controlled-migration of energy in the circuit through a phenomenon called Förster Resonance Energy Transfer (FRET). This, coupled with other unique features of FRET circuits can enable computing in new domains that are unachievable by the conventional semiconductor-based computing, such as in-cell computing or targeted drug delivery. In this thesis, we explore novel FRET-based multiplexing techniques to significantly increase the storage density of optical storage media. Further, we develop analysis algorithms, and computer-aided design tools for FRET circuits.

Existing computer-aided design tools for FRET circuits are predominantly ad hoc and specific to particular functionalities. We develop a generic design-automation framework for FRET-circuit optimization that is not limited to any particular functionality. We also show that within a fixed time-budget, the low-speed of Monte-Carlo-based FRET-simulation (MCS) algorithms can have a potentially-significant negative impact on the quality of the design process, and to address this issue, we

design and implement a fast FRET-simulation algorithm which is up to several million times faster than existing MCS algorithms. We finally exploit the unique features of FRET-enabled optical computing to develop novel multiplexing techniques that enable orders of magnitude higher storage density compared to conventional optical storage media, such as DVD or Blu-Ray.

Dedication

I dedicate this thesis to my father, whose caring support and advice always keeps me motivated, and to my mother, who has always been a role model for me, in diligence and perseverance. I would also like to dedicate this thesis to my uncle, Dr. Koorosh Shahbazi, and my late aunt, Mrs. Fereshteh Mottaghi, who always encouraged me to further my education, and to pursue great goals in my life.

Contents

List of Tables

List of Figures

Acknowledgements

Here, I would like to thank those people whose encouragement, friendship and guidance supported me, while pursuing my Ph.D.

First, and most important, are my parents. Their guidance, support, and care made it easier for me to overcome the hardships of graduate studies. Like my mother, my sister has always been a symbol of self-motivation and perseverance. My father always provided me with caring and enthusiastic support, as well as helpful advice.

Within the Computer Sciences department and the Electrical and Computer Engineering department, many people have influenced me, and unfortunately I cannot list all of them here, but I appreciate their help and contributions.

My advisor, Prof. Chris Dwyer, provided wonderful mentorship and helped me improve many of the skills necessary to perform high quality research. Most importantly, his skills at problem identification, analysis and articulation have had a lasting impact on me. Prof. Jeff Chase has been one of my best mentors. His teaching and presentation style have always inspired me. I would also like to thank Prof. Lebeck, Prof. Sorin, and Prof. Lee for being on my committee.

Finally, all my friends in the ECE nanotechnology group provided a very warm and friendly environment, and without their help it would have been difficult for me to accomplish my research goals. Therefore, I would like to thank all of them; specifically

(in alphabetical order) I would like to thank Arjun Rallapalli, Craig LaBoda, Heather Duschl, Jun Pang, Siyang Wang, Viresh Thusu, and Vishwa Reddy.

1 Introduction

The advent of computers in the 20th century, revolutionized human life and activities, and created opportunities that were hard to even imagine, before. Office automation, electronic banking, electronic commerce, and social media are just few examples of the myriad of such revolutionized domains. Despite this pervasive impact, however, certain domains have not been able to benefit from the potential power of computing, due mainly to the limitations of semiconductor circuits. For example, in targeted drug delivery, it is required that the computational circuitry be sent into cells or biological tissues, and perform computation to identify the places which need treatment, and to determine whether or not to release the drug molecule/packet. The special requirements for computing in these domains which cannot be typically met by semiconductor-based electronic circuitry, have given rise to alternative computing methods such as molecular computing, optical computing, and many more, each of which enables new applications in a particular domain where conventional computing techniques do not apply.

1.1 Design-automation framework for RET networks

The design process in many of FRET applications involves finding the optimum network configuration which minimizes the undesired network behaviors and maximizes the desired characteristics. Since exhaustive search, due to the prohibitively-large size of the design space, cannot address this problem, methodical exploration

approaches are desirable that can find the optimal solution within a reasonable amount of time, by intelligently pruning the search space, and thereby speeding up the search process.

Pruning the FRET-network-design search space, in its general form, is an NP-hard problem, and thus, requires domain-specific heuristics. For this reason, all existing RET-network design methods are ad hoc and specific to certain functionalities (e.g., light-harvesting, wire, etc.). The drawback of these ad hoc methods is their poor design-space exploration capabilities, which is exacerbated by the inherently-slow nature of their design flow.

To reduce the FRET-network design effort, we introduce RETLab, an automated design-space exploration framework that finds the optimum configuration for different RET networks, independent of their functionality. Specifically, different design flows, despite their application-specific nature, share many design steps, and data-processing procedures. By identifying these common functions and procedures, we create a generic design flow in which the functionality aspects of RET-network design are decoupled from its fabrication issues. This enables a uniform design flow to be applicable to all different RET networks, independent of their functionality. Furthermore, by providing a library of frequently-used pre-simulation and post-simulation functions, RETLab reduces the programming effort required to describe the network-specific parts of the exploration.

1.2 Fast FRET-simulation algorithm

The result quality of an automated design flow is influence by many factors, including the approximation rules used in search-space pruning. Specifically, the prohibitively-large size of the design space fuels the inevitable need for search-space pruning which is predominantly implemented using heuristics that are based on locally-valid approximations. These approximations sometimes incorrectly prune regions of the design space that contain high-quality solutions, leading the search process to find only lower-quality results. A high-throughput design flow can mitigate this problem by requiring less search-space pruning (within the same time budget), which in many cases, translates to a lower usage of approximation rules, and thereby, a higher output quality.

While throughput is one of the most important factors that influences the output quality of an automated FRET-network design flow, it is significantly affected by the performance of the FRET simulation algorithm used in the design process, as FRET simulation is an integral part of the design flow, and in most cases, it is the performance bottleneck, limiting the design-process throughput. Currently, all existing FRET simulation algorithms are based on Monte-Carlo methods which are inherently slow. Therefore, a fast FRET simulation algorithm can be an essential part of a high-quality FRET network design process.

To this end, we designed a non-Monte-Carlo FRET-simulation algorithm, called Karoon, which is up to several million times faster than MCS. The high speed of this

algorithm is achieved by avoiding the required statistical sampling in MCS; specifically, all Monte-Carlo methods rely on repeated random sampling from an unknown underlying probability distribution to improve their simulation precision. This repeated process, despite its inherent importance, creates a performance bottleneck for MCS and causes it to be slow. Karoon, on the other hand, has a different view of the energy migration problem in a FRET network, which does not require statistical sampling: unlike MCS, in which the problem is viewed as an *inter-fluorophore exciton migration*, Karoon views the problem as a *population migration* from one network-excitation state[1] to another. Specifically, each exciton-migration scenario is deemed to cause a fraction of the network population at some excitation states to migrate to another state. By pre-calculating all possible inter-state population-migration probabilities, Karoon keeps track of the population-share of every network-excitation state, over the course of simulation. As a result, the number of calculation iterations in Karoon equals the number of excitation states which is typically significantly smaller than the typical number of sampling iterations in MCS, leading to the higher speed of Karoon.

1.3 Techniques for Increasing Optical Storage Density

The demand for high-density digital storage is increasingly growing in the age of digital media, and optical storage techniques (such as DVD and Blu-Ray) have been

[1] For a single fluorophore, two excitation states are possible: *excited* and *unexcited*. For a multi-fluorophore system, a binary vector represents the *network-excitation status* each element of which reflects the excitation status of one of the fluorophores.

among the oldest and most commonly employed to tackle this issue. However, the storage density in these media is limited by the light-diffraction laws, and can only be linearly improved, by reducing the wavelength of the interrogating light and is more practically limited by the availability of laser sources. Therefore, novel storage density enhancement techniques are required to overcome this limitation, and to meet the increasing demand for higher storage densities.

To address this issue, we designed and experimentally demonstrated the PAM-disc, as a high-storage-density medium, which has up to several thousand times higher density. The key idea behind the PAM disc is to store many (e.g., hundreds of) bits in individual cells, instead of the common practice of storing only one or few bits per DVD cell (or pit). To access these bits, we associate each word (collection of bits) with a unique combination of different colors as its address. Therefore, unlike the DVD technology which uses only a single laser color (wavelength) to read data, retrieving data from a PAM disc requires multiple simultaneously incident beams of different wavelengths (colors), and hence the name: Polychromatic Address Multiplexing (PAM). The exponential storage-density increase enabled by PAM originates from the fact that given p available colors, the number of distinct c-color addresses is $\binom{p}{c}$ which grows exponentially in p; for example with only 10 colors, $\binom{10}{5} = 252$ distinct words can be addressed in a single storage cell. Moreover, to further increase the storage density, we

incorporate multi-level recording with PAM to enable retrieving multi-bit words at each address, instead of single-bit words.

1.4 Thesis Contributions and Organization

The focus of this thesis is on the computer-aided design and analysis of FRET circuits, as well as on data-multiplexing enabled by such circuits. Specifically, we make the following primary contributions:

1. We develop and experimentally demonstrate a novel multiplexing technique, called polychromatic address multiplexing, and show its potential applications in increasing optical-storage density, as well as in microscopy.

2. We design and evaluate a new simulation algorithm that is orders of magnitude faster than the conventional simulation algorithms.

3. We develop a design-automation environment for FRET circuits.

4. We design a novel serial multiplexing technique that requires fewer custom-made molecules, and show its potential applications in increasing optical-storage density.

This thesis is organized as follows: In chapter 2, we provide background on FRET circuits and RET logic. In chapter 3, we introduce a FRET-network design automation framework that takes advantage of a fast FRET-simulation algorithm which is described in chapter 4. In chapter 5, we explain our proposal for an optical storage medium with a high storage density, and finally, we conclude in chapter 6.

2 Background: FRET Circuits

FRET circuits are nanoscale molecular ensembles that are operated by light and can perform functions such as sensing, computing, etc. In this chapter we first introduce the physical phenomena that underlie FRET circuits, and then we explain how FRET circuits work.

2.1 Fluorescence

Fluorescence is the light-driven emission of light by certain substances which are called fluorescent materials. It is a form of photoluminescence which refers to cold body radiation due to the absorption of light. As a result of fluorescence, the fluorescent substance emits light that has a different color (i.e., energy) than the absorbed light. For example, Figure 2-1 shows three different fluorescent materials all of which are illuminated by the same UV light (invisible), but each fluorescing in a different color. This experiment demonstrates that upon the absorption of an incident-photon by the fluorescent substance, a new photon (often, with lower energy) is generated, because here, the incident light does not have any visible photons.

Figure 2-1 – Fluorescence: all the three liquids are excited with UV, but each emits at a different wavelength.

2.1.1 Physics of fluorescence

Fluorescence occurs when a photon is emitted due to the relaxation of an excited orbital electron. The molecular (or crystal) structure of fluorescent materials is such that the excitation band gap of some of their orbital electrons matches the energy of photons in the UV-Visible-IR range. As a result, a photon with sufficient energy (and appropriate polarization) can bring these orbital electrons to excitation. Once an orbital electron is excited, an excess amount of energy (supplied by the incident photon) is temporarily stored in the molecule which can be dissipated through several pathways, one of which is the radiative pathway of fluorescence. The following two equations summarize the excitation and fluorescence processes:

Excitation: $S_0 + h\nu_{ex} \rightarrow S_1$
Fluorescence: $S_1 \rightarrow S_0 + h\nu_{em} + E_{nondiative}$

The energy of the absorbed photon brings the molecule to the first electronically-excited singlet state (denoted by S_1). Some fraction of this energy is dissipated non-radiatively ($E_{nonradiative}$) and the remainder forms a photon with lower energy ($h\nu_{em}$) as

the molecule relaxes back to its ground state (denoted by S_0). These processes can also be illustrated by an energy diagram called the Jablonski diagram which is shown in Figure 2-2.

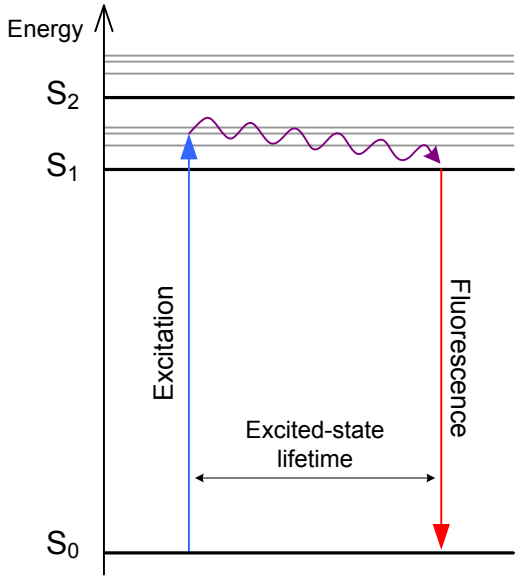

Figure 2-2 – Jablonski energy diagram of fluorescence

Phosphorescence is a similar photoluminescence process which is different from fluorescence in the relaxation mechanism, as it involves a triplet-state conversion during de-excitation, before reaching the ground state, i.e., $S_1 \rightarrow T_1 \rightarrow S_0$.

2.1.2 Excitation and Emission Spectra

Light absorption by some fluorescent molecules is higher than others due mainly to their molecular structure. Moreover, the same fluorescent molecule absorbs light more strongly at some wavelength than at others. The *extinction coefficient* (denoted by ϵ) of a molecule determines how strongly that molecule absorbs light at a given

wavelength. The excitation spectrum of a fluorescent molecule reflects how strongly that molecule is excited at different wavelengths. Figure 2-3 shows the excitation spectra of two fluorescent dyes (i.e., fluorophore types). As shown in the figure, the maximum extinction coefficient (denoted by ϵ_{max}) of these two dyes occurs at two different wavelengths (λ=493nm and λ=591nm); further, $\epsilon_{max}(AF488) > \epsilon_{max}(AF594)$ which indicates that AF594 is a stronger light absorber at λ=591nm than AF488 is at its absorption peak (i.e., λ=493nm).

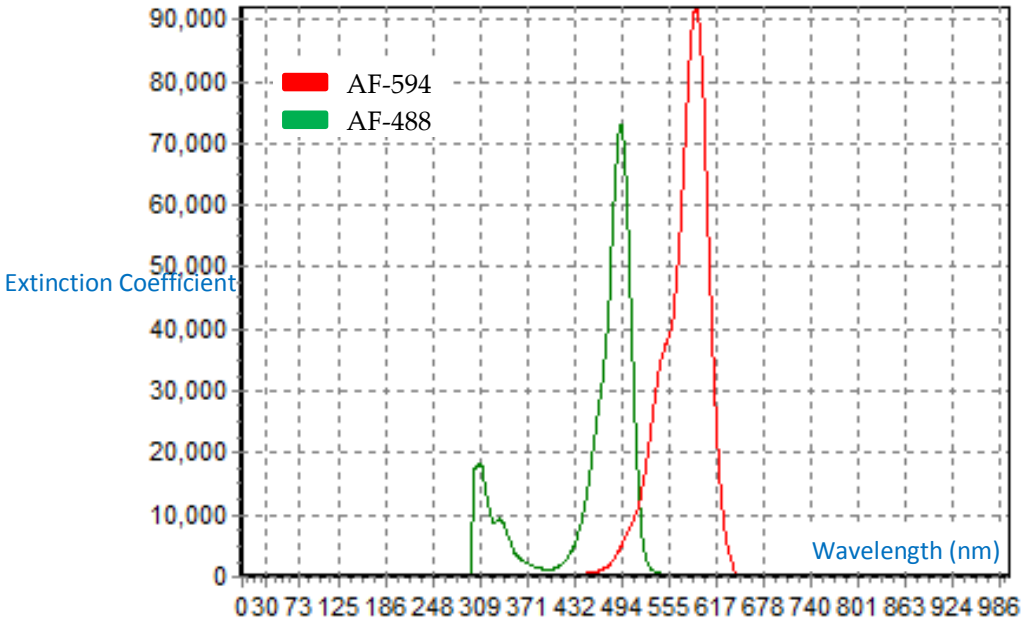

Figure 2-3: Excitation spectra of two fluorescent molecules: different molecules are differently excited by light

It is important to note that in general absorption and excitation spectra might not be the same; because the excitation spectrum is measured by change in the fluorescence intensity as a function of the excitation wavelength; whereas the absorption spectrum is

the decrease in the intensity of light as it passes through the sample, as a function of its wavelength. The difference originates from the fact fluorescence emission often occurs from S_1 and some molecules can be excited to higher excitation sates (e.g., S_2 or S_3) from which they can directly de-excite to the ground state without any emission. In such cases, even though the molecule exhibits, high absorption, it does not exhibit high fluorescence, causing the two spectra not to be the same.

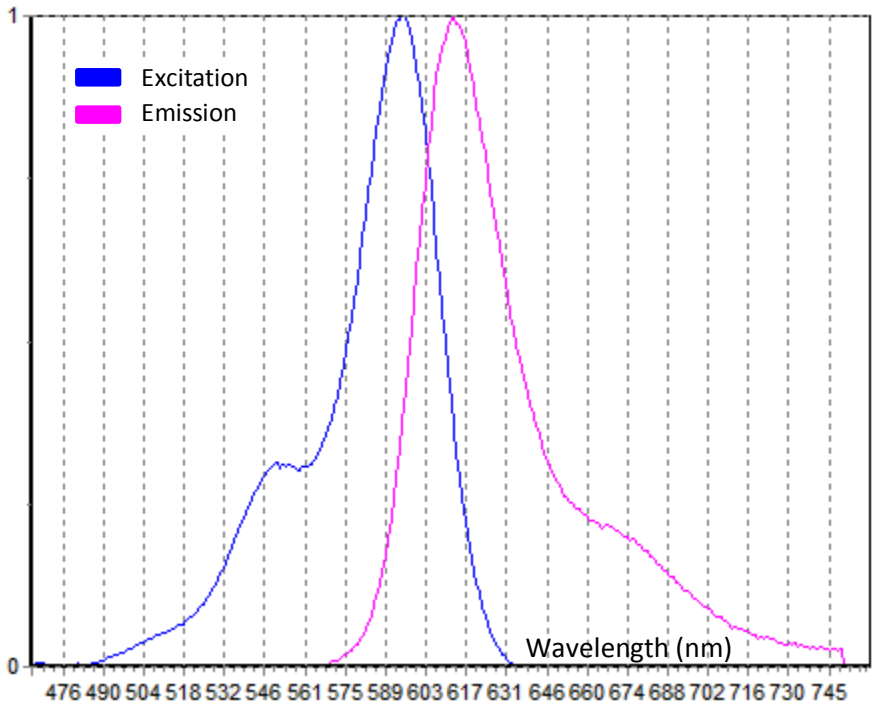

Figure 2-4: Normalized Emission- and Excitation spectra of Texas Red

In addition to not being equally-sensitive to different excitation wavelengths, dyes do not equally fluoresce at different wavelengths, either. Specifically, each dye, depending on its molecular structure, fluoresces at different wavelengths with different probabilities which are revealed by its emission spectrum. For example, as shown in

Figure 2-10, TexasRed (which is an aromatic dye) has an emission peak at 610nm indicating that the fluorescence wavelength of this dye is more likely to be around 610nm. The emission spectrum of a dye is extracted by exciting a dilute solution of the dye at a fixed wavelength, and measuring the relative fluorescence (emission) intensity at different wavelengths using a monochromator (e.g., a prism).

2.2 Förster Resonance Energy Transfer

Förster Resonance Energy Transfer (FRET) is the non-radiative transfer of energy from an *excited* molecule (donor) to a nearby *unexcited* molecule (acceptor) through dipole-dipole coupling. FRET, which typically occurs at < 10nm donor-to-acceptor distances, enables a fluorescent molecule (also called a *fluorophore* or a *chromophore*) to be excited by wavelengths outside of its excitation spectrum; for example, in Figure 2-5 two sufficiently-far-apart fluorophores (i.e., CFP and YFP) are both illuminated by 436nm wavelength light, but only CFP is fluorescing (at 480nm); however, when CFP and YFP are close to each other (Figure 2-6), another emission peak is observed (at 535nm); this indicates that YFP is being excited through CFP, because the excitation wavelength is still 436nm, which is not well-absorbed by YFP.

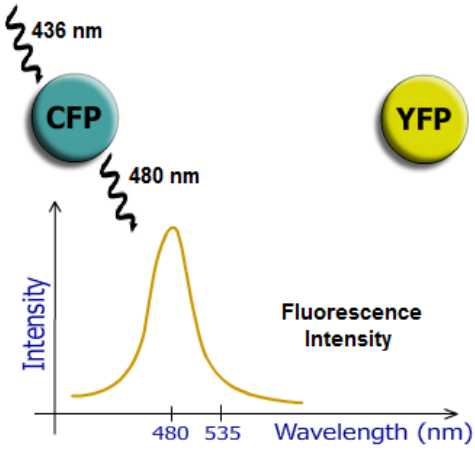

Figure 2-5 – NO FRET: Only CFP is excited and since YFP is too far from CFP, no FRET happens; hence YFP does not fluoresce.

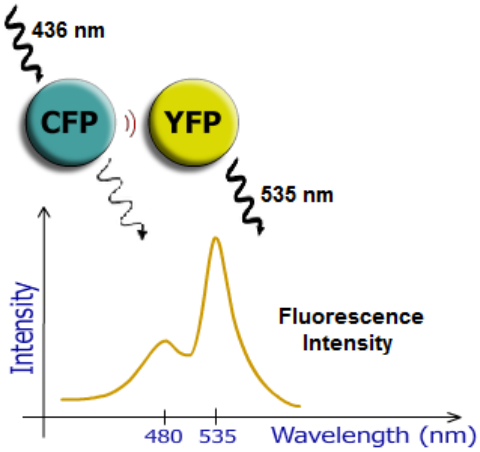

Figure 2-6 – FRET: Only CFP is excited but YFP also fluoresces; since it receives energy from CFP (due to FRET).

2.2.1 Physics of FRET

FRET is enabled by the Coulombic interaction between two oscillating molecular dipoles, due to which the oscillations in one dipole (under certain conditions) induce resonance in the other dipole, and thereby cause the energy transfer to that dipole. The oscillations in the dipoles are enabled by delocalized electrons in the molecular structure of the fluorophore, which are usually due to overlapping π-orbitals.

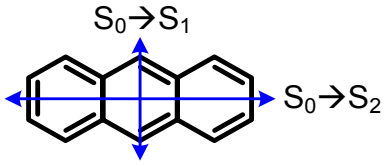

Figure 2-7 – Aromatic compound with alternating c-c and c=c: in this molecule, π-electrons are delocalized over the entire molecule

The existence of alternating single and double carbon-carbon bonds extends the π-electron system, which in turn, decreases the required energy for promoting an electron in such orbitals. As a result, the alternating electric field of an incident photon (at the right wavelength) can induce transient charge displacement in the molecule by temporarily dislocating an electron and thereby promoting it to an excited state (e.g., S_1). This charge displacement creates a transient dipole which can be represented by a transition moment as shown in Figure 2-7. In this figure, the moment of transition from S_0 to S_1 is along the short axis, and the S_0-to-S_2 transition moment is along the long axis of the molecule.

2.2.1.1 Dipole-Dipole Interaction

The classical-physics view of the dipole-dipole interaction can be described by the Coulombic charge interaction laws. The charge displacement induced on the excited molecule, creates a transient oscillating dipole (as the molecule attempts to return to its ground state) which can in turn induce an oscillation on a nearby molecule, as illustrated in Figure 2-8. In this figure, the transient negative charge concentrated on the left ring of the excited donor repels away (through exertion of Coulomb force) the negative charge in the acceptor molecule, inducing a dipole on the acceptor.

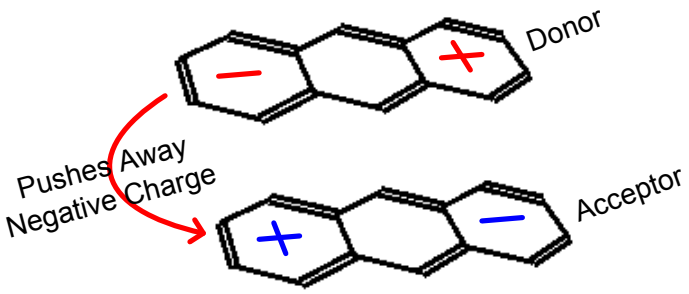

Figure 2-8 – Dipole-Dipole Interaction: the dipole created at the donor induces a charge displacement on the acceptor through Coulombic interaction

The oscillation of the donor dipole imposes an oscillation on the acceptor which can cause resonance in the acceptor and consequently excite it. The mutual alignment of the dipoles (denoted by κ^2) affects the efficiency of FRET. Furthermore, other factors such as the medium between the donor and acceptor, excitation band gap of the acceptor, etc. can also affect the transfer efficiency, which will be discussed later.

2.2.2 Transfer Efficiency

Similar to fluorescence, FRET is also one of the relaxation pathways that simultaneously compete with one another to de-excite an excited fluorophore, and its efficiency (denoted by η) is defined to be the ratio of transfer events over the total excitation events, as expressed in the following equation:

$$\eta = \frac{\#\ transfer\ events}{\#\ donor\ excitation\ events} = \frac{1}{1+\left(\frac{r}{R_0}\right)^6}$$

As inferred from this equation, the efficiency of RET strongly depends on the donor-to-acceptor distance (denoted by r), and the Förster radius of the RET pair (denoted by R_0).

Förster radius (R_0) which is the distance at which η=50%, typically ranges between ~3.5nm and ~8nm, and depends primarily on the molecular structure of the donor and acceptor. Specifically, R_0 depends on the overlap integral of the donor emission spectrum with the acceptor excitation spectrum, as well as the relative orientation of the dipoles (denoted by κ^2) and the refractive index of the medium (denoted by n), as expressed in the following formula:

$$R_0{}^6 = \frac{9(\ln 10)}{128\pi^5 N_A} . \kappa^2 n^{-4} J Q_0$$

Q_0 is the intrinsic quantum yield of the donor (explained later), and J is the spectral overlap integral calculated using the following equation [1], wherein $\overline{f_D}$ is the normalized f_D (i.e., fluorescence (emission) spectrum of the donor), and $\epsilon_A(\lambda)$ is the molar extinction coefficient of the acceptor at wavelength λ:

$$J = \int \overline{f_D}(\lambda)\epsilon_A(\lambda)\lambda^4 \, d\lambda = \frac{\int_0^\infty f_D(\lambda)\epsilon_A(\lambda)\lambda^4 \, d\lambda}{\int_0^\infty f_D(\lambda) \, d\lambda}$$

The orientation factor, κ^2, ranges between 0 and 4. For freely rotating fluorophores, the average value of 2/3 is usually used, and for hindered rotors (e.g., fluorophores attached to a DNA strand) a wobbling-in-cone model is used to calculate the average value of κ^2 (which is typically < 2/3) based on the degree of rotation restriction.

2.2.2.1 Intermolecular Transfer Efficiency in Free-Dye Solutions

RET-network solutions might contain freely diffusing dye molecules (free dyes) which at high concentrations can form parasitic RET paths (pairs) with network nodes

(chromophores) and interfere with the operation of the network inducing some unwanted behavior in the network; therefore it is important to know the maximum allowed concentration of free dyes for proper operation of the network. Here we calculate the transfer efficiency of parasitic RET paths as a function of free-dye concentration.

Assuming free dyes are evenly distributed in the solution we first need to know how far the network node is from a free dye molecule. The number of free dye molecules (n) in a spherical volume (radius: r) around the node is given by the following formula:

$$n = concentration \times N_A \times volume = cN_AV = cN_A \times \frac{4}{3}\pi r^3 \times 1000$$

We define ρ to be the radius at which n=1; i.e., only a single free dye molecule is in the sphere. This radius is the average distance to the nearest interacting free dye molecule (i.e., the strongest FRET pair), and thus, n=0 for any smaller sphere ($r < \rho$).

$$r = \sqrt[3]{\frac{3n}{4000\pi N_A c}} \overset{n=1}{\Longrightarrow} \rho = r = 0.1 \times \sqrt[3]{\frac{3}{4\pi N_A c}}$$

Now, using R_0 we can calculate the transfer efficiency: $TE = \frac{1}{1+\left(\frac{\rho}{R_0}\right)^6}$

Figure 2-9 show ρ at different concentrations. As seen in the figure, at low concentrations (< 50nM), ρ is greater than 20nm which is too large for most FRET pairs to have a considerable transfer efficiency; since R_0 typically ranges between ~4 to ~8 nm for most FRET pairs.

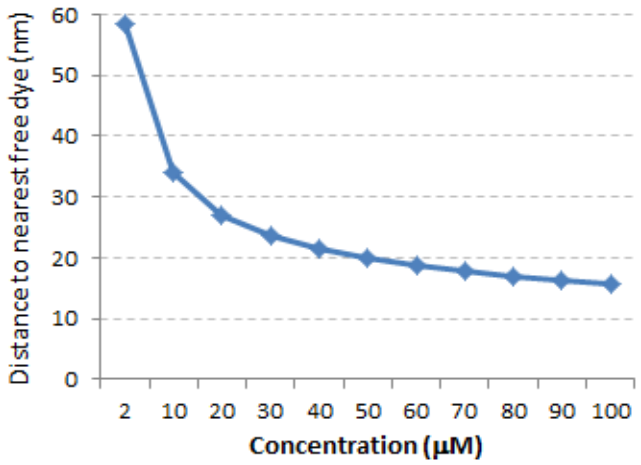

Figure 2-9 – Distance from a fixed molecule to the closest freely diffusing molecule at different concentrations – At <50µM concentrations, this distance is greater than 20 nm.

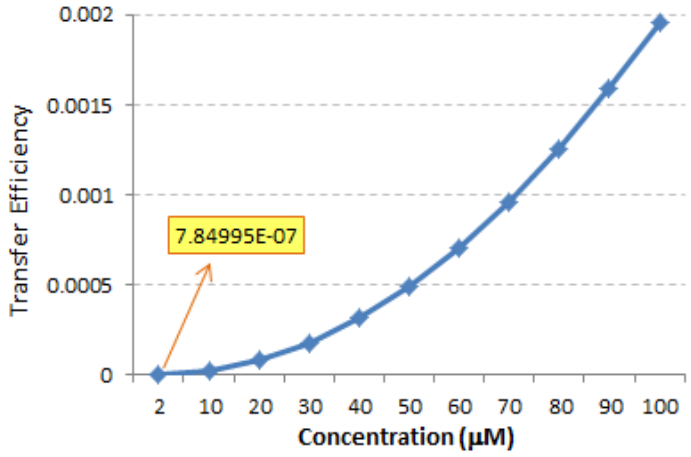

Figure 2-10 – FRET efficiency from a fixed donor (AF-488) molecule to freely diffusing acceptor molecules (AF-647) at different concentrations – At low concentrations (< 50uM) the transfer efficiency is negligible.

Figure 2-10 shows the transfer efficiency from a fixed AF-488 molecule to free AF-647 molecules (R_0 = 5.6 nm) at different concentrations. At 50µM the transfer efficiency is only 0.0005, which is negligible.

2.3 Kinetics

Kinetics is the study of de-excitation rates. Most of the de-excitation processes follow first-order kinetics, meaning that they only depend on the concentration of the excited state population. For example, in a *dilute* solution of fluorophore D, if a δ-pulse at time t=0, creates an excited D-population, then fluorescence competes with other non-radiative pathways to *depopulate* the excited population as described by the following equation, in which k_F and k_L denote the rate constant of fluorescence and non-RET quenching[2], respectively, and [D*] is the concentration of the excited D fluorophores:

$$\frac{d[D^*]}{dt} = -[D^*](k_F + k_L) \qquad (2\text{-}1)$$

In the presence of FRET, the above equation is augmented with k_R, which denotes the rate constant of FRET, to describe the competition between FRET and other quenching pathways:

$$\frac{d[D^*]}{dt} = -[D^*](k_F + k_L + k_R)$$

2.3.1 Lifetime

The fluorescence lifetime refers to the average time that an excited fluorophore stays in the excited state before relaxing back to the ground state. The *intrinsic*

[2] Quenching refers to any de-excitation mechanism that decreases the intensity of fluorescence by competing with it to depopulate the excited population.

fluorescence lifetime of a dye[3] is its fluorescence lifetime in the absence of FRET, which is denoted by τ_0 and can be derived from Eq.2-1. Specifically the solution to this equation is $D(t) = I_0 e^{-(k_F+k_L)t}$ wherein D(t) denotes [D*] at time t and I_0 is the initial excited population created at time t=0. The inverse of this function yields the time at which the excited population has a given size, i.e. $t(D) = D^{-1}(t) = -\frac{\ln(D)-\ln(I_0)}{k_F+k_L}$. Taking the average of the inverse function yields τ_0 as follows:

$$\tau_0 = \text{Avg}\big(t(D)\big) = \frac{\int_0^{I_0} t(D)\, dD}{I_0 - 0} = \frac{1}{I_0}\int_0^{I_0} -\frac{\ln(D) - \ln(I_0)}{k_F + k_L} dD = \frac{1}{I_0}\left(\frac{I_0}{k_L + k_F}\right) = \frac{1}{k_L + k_F}$$

Therefore, the intrinsic fluorescence lifetime of a fluorophore is $\tau_0 = \frac{1}{k_L+k_F}$ which is also the time that it takes for the excited population to reach 1/e (i.e., ~37%) of its initial size. The value of τ_0 primarily depends on the molecular structure of the fluorophore, however, it can also be affected by micro-environmental factors such as solvent viscosity, pH, temperature, etc.

2.3.2 Quantum Yield

Some dyes, even when excited at their maximum extinction coefficient wavelength, still have lower fluorescence intensity compared with others. This can be caused either by low absorptivity or by low fluorescence rate (or both); specifically, in these dyes the fluorescence process might occur at a much slower rate than quenching

[3] The term *dye* is often used to mean a fluorophore *type* which is merely responsible for photophysical properties, and to particularly indicate that the fluorophore *position* relative to other molecules is not important.

processes, causing the majority of the excited population not to contribute to the fluorescence intensity by being quenched instead. The intrinsic *quantum yield* (denoted by Φ_0) of a dye is a measure of its fluorescence efficiency and is defined as the ratio of emitted- to absorbed photons (in the absence of FRET):

$$\Phi_0 = \frac{\#\ emitted\ photons}{\#\ absorbed\ photons} = \frac{k_F}{k_F + k_L}$$

The intrinsic quantum yield of a dye can be affected by the solvent, temperature, pH and other micro-environmental factor, as well as its molecular structure.

2.4 FRET Circuits and Implementation of Logic Functions

FRET circuits are supramolecular complexes composed of several fluorophores that intercommunicate through FRET, and can perform various functions such as computing, sensing, etc. In most FRET circuits it is usually required that certain inter-fluorophore distances be fixed, and therefore, the constituent fluorophores are often covalently bound to an underlying nanostructure (e.g, a DNA grid[2], or a protein) which serves as a scaffold and enforces the required inter-fluorophore separations. A RET device is usually composed of a relatively large population (e.g., 250 nano moles) of these multi-fluorophore structures which collectively implement a logic function.

The absorption and emission of photons by chromophores can serve as the input and output mechanisms, respectively. Signal separation is achieved by wavelength division multiplexing (WDM) in the same physical medium (channel). For example, Fig. 2-11 shows an OR gate in which two different dyes are used for A and B and therefore, each

one becomes excited by a different wavelength ($\lambda_{ex(A)}$ and $\lambda_{ex(B)}$). The communication is enabled by RET, the rate (strength) of which can be tuned by adjusting the donor-to-acceptor distance, or the choice of corresponding dyes. In the OR gate example (Fig. 2-11), A and B have RET to O and therefore an exciton in either one of them hops to O and eventually fluoresces out (at λ_O) which can be detected by a photo-detector.

In general arbitrary logic functions can be implemented by controlling the *exciton flow* within a RET network, which is achieved by either engineering pairwise RET rates, or saturating acceptors. The rate constant (k_R) of a RET pair depends non-linearly on the donor-to-acceptor distance (i.e., r) as well as their molecular structures as expressed by Eq.2 [1]:

$$k_R = \frac{1}{\tau_0}\left(\frac{R_0}{r}\right)^6 \qquad (2)$$

In this equation, R_0 is called the Förster radius which is the distance at which half of the excited donors transfer to their acceptors[1]. Depending on their molecular structure, different donor-acceptor pairs have different R_0 values. Further, τ_0 is the intrinsic excited-state lifetime of the donor.

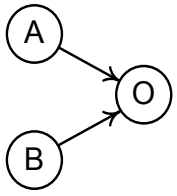

Fig. 2-11. A RET network that implements a two-input RET-logic OR gate – Node O is the output and fluoresces (emits photons) if excitons from A or B hop to O through RET.

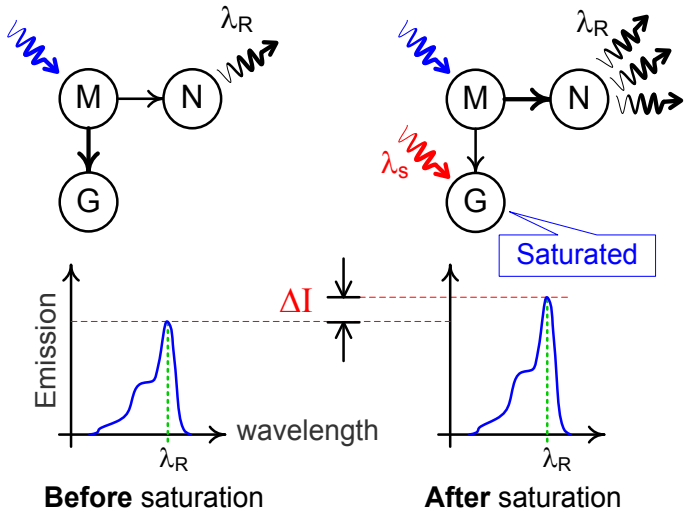

Fig. 2-12. Saturation of G weakens the M→G path and increases the fluorescence of N

Another exciton-flow control mechanism is acceptor saturation which can be achieved by *intensely* exciting the acceptor either through another donor or directly by incident photons. Acceptor saturation occurs because *only a single* exciton can excite an unexcited chromophore, and no excitons can hop to an already-excited chromophore [3]. This implies that when multiple excitons attempt to hop to the *same* acceptor simultaneously, *exciton collision* occurs as a result of which only one exciton hops, while others remain unmoved. In Fig. 2-12 for example, nodes G and N compete to depopulate the excited M population. The saturation of G induces an increase on N's share of hopping excitons from M, because after being saturated, G receives fewer excitons from M, leaving more excitons available for N to receive per unit time.

3 FRET-Circuit Design Automation Framework

One of the drawbacks of existing RET-network design methods is their low throughput which, with a limited design time, translates to poor and coarse-grained exploration of the design space. The key to overcome this problem is higher throughput which we have achieved by making two modifications to existing RET design flows: first, we have added a *validation* step before the evaluation step, which quickly identifies disqualified configurations without thorough simulation. Second, we have developed a new evaluation algorithm which is faster than existing evaluation algorithms.

3.1 Proposed Design Approach

A trivial approach to solve the dye-and-site assignment problem is the exhaustive search; i.e., to evaluate every single possible combination of dyes and sites and to choose the best. Despite being easy, this approach does not scale beyond two or three chromophores. For example, currently there are ~300 commercially available dyes. Hence, the design space for a 3-chromophore network has $\binom{300}{3} \times \binom{192}{3} \approx \sim 5\text{x}10^{12}$ combinations, assuming a total of 192 possible sites. For a 4-chromophore network, the size of the design space grows to ~$2\text{x}10^{16}$. Therefore, full exploration of the design space is practically impossible, due to its prohibitively large size, motivating the need for incorporating pruning techniques into the design flow.

3.1.1 Observations

Comparing two different near-optimal dye-site assignments requires detailed time-resolved simulation of the RET networks which is typically slow, ranging from milliseconds to hours, depending on the network. However, we have observed that it is often very easy to disqualify an assignment by a quick inspection and without simulation. For example, in the OR gate of Fig. 2-11, both A and B must have RET to O which requires that $\lambda_{ex(A)} < \lambda_{ex(O)}$ and $\lambda_{ex(B)} < \lambda_{ex(O)}$. Therefore, any given assignment that does not satisfy any of these two rules can be ignored without simulation. Checking these rules is three to four orders of magnitude faster than physical simulation.

The second observation is that, not only is it possible to avoid simulations, but sometimes it is also possible to avoid even quick inspections by pruning the search space. For example, in Fig. 2-11 the assignment vector has six elements, three dyes and three sites $<D_a, D_b, D_O, S_a, S_b, S_O>$. By a quick inspection we can disqualify assigning *RR* and *LY* (two commercial dyes) to B and O respectively. After this inspection, all subsequent assignments of the form <x,***RR***,***LY***,x,x,x> are also disqualified without even being inspected, because they all contain the invalid assignment. Therefore, depending on the nature of the target function it might be possible to prune the search space based on the history of quick inspections.

Based on these observations we have developed a design flow that is independent of the target logic function and enables exploration of larger design spaces (i.e., more dyes and sites) by avoiding unnecessary (and time consuming) simulations.

3.1.2 Overview

As illustrated in Figure 3-1, the proposed design flow involves user-guided sampling of the design space followed by validation of each sample to check if it qualifies for a potential solution (candidate). In this figure, the design space is the set of all possible dye-site assignment vectors and the sample space is a subset of the design space for every vector of which a quick inspection is performed. Those vectors out of the sample space which pass the validation test (quick inspection) form the candidate space. To find the final solution, all (or some) candidates are fully simulated, from the results of which the values of a set of user-defined metrics are extracted. Finally the candidates are ranked based on these metrics and the best ones are chosen as the solution(s).

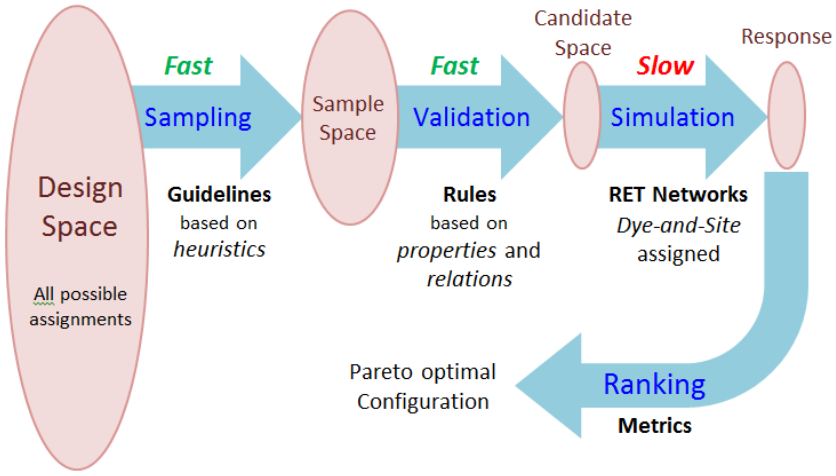

Figure 3-1: Overview of the proposed design flow – four major steps: sampling, validation, simulation and ranking

The speed and quality of the design process can be significantly influenced by the sampling step in Figure 3-1, as for example a smaller sample space can be inspected faster. The sampling technique is domain specific and cannot be automatically found; however, the rules and guidelines that describe it can be broken down to a set of properties and relations which are common among many different sampling techniques. We have identified and implemented a set of frequently used properties and relations, and accordingly have provided a library of functions that can serve as building blocks for describing arbitrary domain-specific sampling techniques. Using these functions, designers can easily express their domain-specific heuristics at a higher level to guide the sampling such that *only* those regions of the design space that are likely to contain a candidate, are sampled.

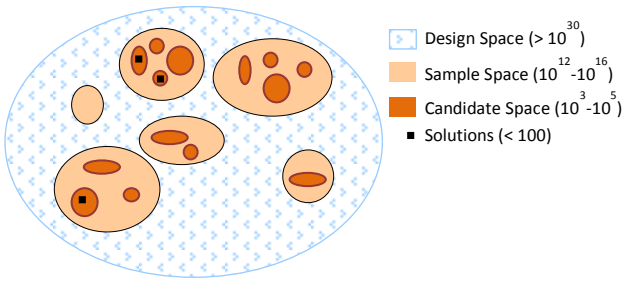

Figure 3-2: Relative size of the design space vs. sample space and candidate space – Most regions of the design space are not inspected (sampled).

By incorporating the two fast steps of sampling and validation into the design flow, the proposed approach enables more sites and dyes to be explored per unit time, as more pruning yields a smaller sample space and thereby a faster design cycle. Figure 3-2 shows the typical relative size of these spaces for an 8-chromophore network.

3.2 Design Flow

Figure 3-3 illustrates the details of the design flow. As seen in this figure, the inputs to the design problem are the target logic function and the set of available dyes and sites. The target logic function is described for *RETLab* in the form of an exciton flow graph (EFG) which is constructed based on the principles of RET logic and the functionality of the target function. In addition to these, the automated design flow also requires extra domain specific information which can be classified into *Guidelines*, *Rules* and *Metrics*. These three classes of information are used by different tools of *RETLab* to find the optimal RET network. Extraction of this information requires domain expertise and human intelligence and cannot be automated.

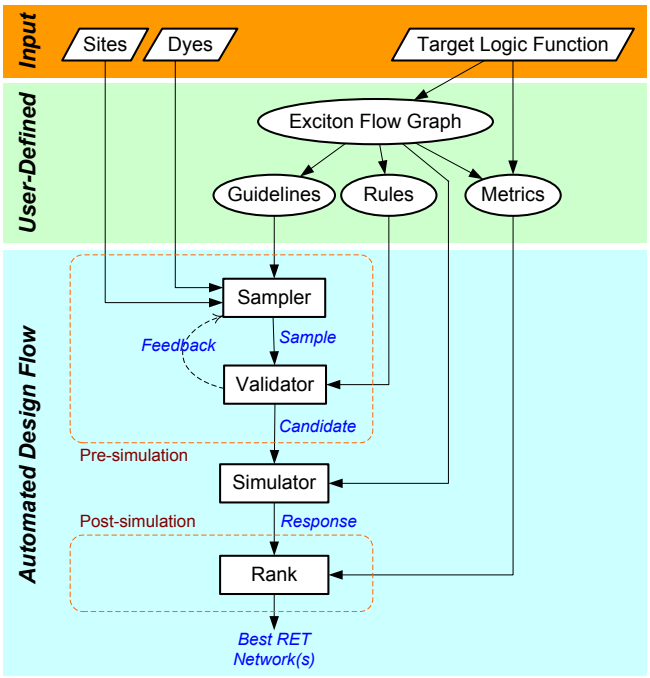

Figure 3-3: Design flow used in RETLab

3.2.1 Guildelines

As depicted in Figure 3-2 and Figure 3-3, the design process requires an efficient pre-simulation pruning of the design space. The pruning algorithm is described and implemented using guidelines which direct the flow of sampling, as well. The quality of the sampling depends on the underlying algorithm, for example the two samplings in Figure 3-4 both yield the same sample space, but the first algorithm requires only ~64 thousand rule evaluations whereas the second requires ~1.3 million; this is because in sampling-1 the input and output chromophore spaces are first pruned and then *paired*, whereas in sampling-2 they are paired without any initial pruning. This example demonstrates how significantly a pruning algorithm can affect the design process performance.

3.2.2 Rules

Design rules describe conditions that disqualify a dye-site assignment without simulation. They can also be used to direct the sampling. For example, a minimum or maximum required distance between two nodes in the network can be declared as a spatial design rule. As another example, one of the design rules in Figure 3-4 has been highlighted. Since the mathematical description of design rules is based on a set of attributes that can be determined without simulation, they can be quickly evaluated. Some of these attributes include *Intrinsic Fluorescence Lifetime, Extinction Coefficient, Quantum Yield, Spectral Separation, Förster Radius (R0), and Transfer Efficiency* [4].

3.2.3 Metrics

Extracted from simulation results, metrics are behavioral attributes of a RET network that are used to rank simulated networks. The simulation provides time-resolved details about the evolution of the excited population at each node as well as its fluorescence, RET, etc. The designer provides procedures to extract the value of each metric from the simulation results. For example, *gate delay* and *noise margin* are two metrics based on which the best RET network can be selected.

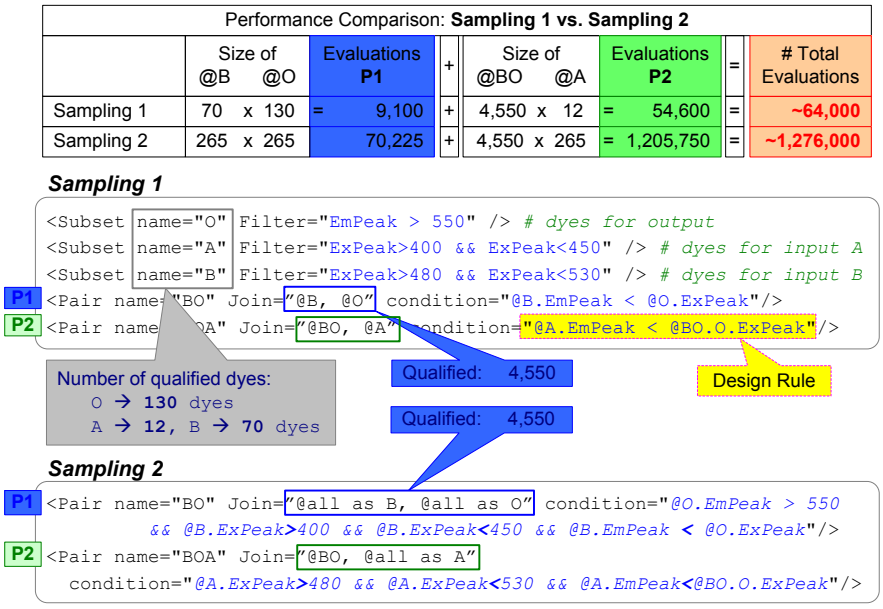

Figure 3-4: Example for guidelines and design rules implementing two different sampling algorithms that generate the same sample space – Both algorithms generate a triplet set (called *BOA*) from a pair set (called *BO*); however, Sampling 1, starts pairing from smaller sets (B, O and A) whereas Sampling 2, starts pairing directly from the set of all available dyes (called *@all*). – Each *Pair* operation involves *n1* x *n2* evaluations where *n1* and *n2* are the size of source sets. Therefore Sampling 1, causes far fewer evaluations, hence runs faster. – Set *@all* in this example contains 265 commercially available dyes.

4 Karoon: A fast and precise FRET-simulation algorithm for partially-saturated multi-fluorophore networks

Resonance Energy Transfer (RET) is classically described by first-order kinetics. Although this model (i.e., classic model) can be easily generalized to a network of interacting fluorophores, it does not apply to networks in which multiple donors compete to excite a shared acceptor. Thus, to obtain accurate results in such cases, Monte-Carlo simulation (MCS) is used to simulate energy migration in the network, based on a competition-aware model. In this chapter, we introduce a new RET simulation algorithm, called Karoon, which is up to several million times faster than MCS, and unlike MCS, does not require any network-specific precision-enhancement techniques. The higher speed and precision of this algorithm enables a more comprehensive computer-aided RET-network design. Additionally, for the competition-aware model that underlies MCS, we present a new mathematical description based on a system of inhomogenous and time-variant ordinary differential equations which enables deterministic- and thereby highly precise analysis of RET network behaviors. We finally, validate our algorithm with various experimental data.

4.1 Introduction

Förster Resonance Energy Transfer (FRET or RET) is the non-radiative transfer of energy through dipole-dipole coupling from an excited- to an unexcited fluorophore (i.e., donor to acceptor)[4]. This phenomenon has been increasingly employed in a wide

range of domains and applications. In fact, in addition to its extensive use in the study of protein conformation and interactions[5], cellular structures[6], metabolic pathways[7], and cell membranes[8] (super-resolution microscopy), FRET has also been used in sensing[9, 10], light harvesting[11], self-organizing computer architectures[12], enhancing organic lasers[13], implementing logic circuits[14] (RET logic), as well as many other important applications.

The design process in many of these applications involves analyzing the response of a network of fluorophores which interact through RET[5, 10]. The kinetics of energy migration in a RET network is classically described by a system of ordinary differential equations (ODE), wherein each RET path is described by first order kinetics, using a single rate constant[15]. This model is only valid as long as the excited-state mutual exclusion holds for all the RET pairs in the network; meaning that the donor and acceptor of any given RET pair can never be simultaneously excited in this model[16]. Therefore, a RET network with acceptors that are shared by multiple donors, cannot be analyzed using the classical model, because these acceptors can violate the mutual exclusion requirement by becoming excited through one of their donors while another is still excited. In such cases, energy migration in the network is often simulated using a Monte-Carlo method[17-20] based on an alternative model which accounts for the competition among multiple donors sharing a single acceptor[3, 17, 18].

Despite its flexibility, MCS has the drawback of trading off speed for precision, causing it to be significantly slower than deterministic methods for solving ODE's, and thereby rendering it almost impractical to be used in certain applications such as RET-circuit design[14]. This inherent drawback is because Monte-Carlo methods, in general, rely on a statistical sample which has to be sufficiently large to yield the desired precision. Another disadvantage of MCS is that in the case of rare events (e.g., a fluorophore that rarely receives excitons), domain- or network-specific sampling techniques have to be applied to enhance the otherwise-poor precision of the simulation[18, 20, 21], making MCS less general, and not applicable to *arbitrary* networks without modifications.

In this work, we have developed a new RET simulation algorithm, called Karoon, which is – at the cost of higher memory usage – several orders of magnitude faster than MCS, and yet highly precise. Further, unlike MCS, it can simulate any arbitrary network without requiring network-specific modifications. The other contribution of this work is introducing an ODE-based description for the non-classical model used in MCS which enables deterministic and parametric analysis of RET circuits. This mathematical description can also be easily generalized to incorporate other important physical phenomena in RET networks, such as photo-bleaching, exciton-annihilation mechanisms, etc.

4.2 Background: Kinetics of Energy Migration

In this section we review the classical model for describing energy migration in multi-fluorophore structures. For the sake of brevity, we do not consider exciton annihilation mechanisms such as triplet-triplet annihilation – which typically occurs at high concentrations – and singlet-singlet annihilation. Furthermore, among energy transfer mechanisms we only consider the singlet-singlet energy transfer as shown in the following formula.

$$^1\boldsymbol{D}^* + {}^1A \rightarrow {}^1D + {}^1\boldsymbol{A}^*$$

4.2.1 Single RET pair

In a dilute solution of D fluorophores, every single molecule of which is bound to an unexcited acceptor at distance r, if a fraction of the D population is excited at time t=0 by a δ-pulse, the following differential equation describes the decay of the excited population of D molecules[4].

$$\frac{d[D^*]}{dt} = -[D^*](k_F + k_L + k_R) \qquad (4\text{-}1)$$

In this equation, [D*] denotes the concentration of *excited* D fluorophores, k_F and k_R are the rate constants of fluorescence and RET respectively, and k_L is the sum of all other de-excitation (exciton loss) rate constants. These rate constants can be calculated from Φ_0 and τ_0 (measured experimentally) using the following formulae in which Φ_0 is the quantum yield of D, and τ_0 is its intrinsic excited-state lifetime in the absence of any acceptors (absence of RET).

$$k_F = \frac{1}{\tau_0}\Phi_0$$
$$k_L = \frac{1}{\tau_0}(1-\Phi_0)$$
$$k_R = \frac{1}{\tau_0}\left(\frac{R_0}{r}\right)^6 \qquad 4\text{-}2$$

The above formulae are derived from the definitions of Φ_0 and τ_0, namely $\tau_0 = \frac{1}{k_F+k_L}$ and $\Phi_0 = \frac{k_F}{k_F+k_L}$ and the calculation of k_R follows from Förster's formula, namely $TE = \frac{k_R}{k_F+k_L+k_R} = \frac{1}{1+\left(\frac{r}{R_0}\right)^6}$ wherein r denotes the D-to-A distance (A is the acceptor molecule), and R_0 is the Förster radius of the D→A RET pair[4, 22]. We call k_R (given by Eq.4-2) the *nominal* RET-rate constant of the D→A pair, as it might overestimate (explained later) the *effective* RET-rate constant.

4.2.2 RET with Partially-Saturated Acceptors

The exciton transfer from D to A in Eq.4-1 is based on the assumption that for every excited donor molecule, an *unexcited* acceptor molecule exists. This assumption however, might not always hold; specifically the corresponding acceptor molecule can be already excited and not accepting any more excitons from the donor, changing the calculation of RET as illustrated in Figure 4-1.

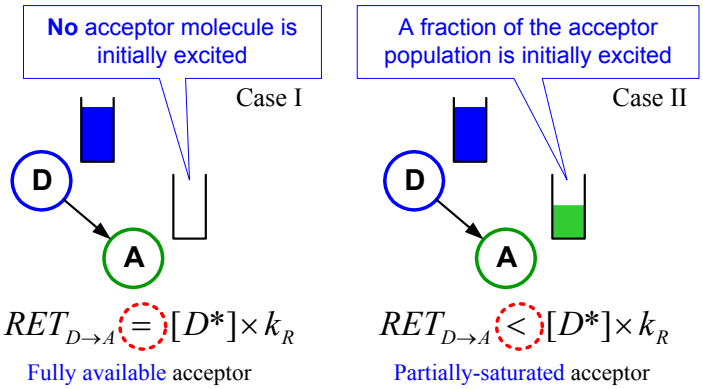

Figure 4-1 – Effect of acceptor pre-excitation on RET – In case I, no acceptor molecule is initially excited, hence [A] is fully available to quench [D*] and $\boldsymbol{RET_{D\to A} = [D^*] \times k_R}$. But, in case II some fraction of the acceptor population is excited before the donors are excited and consequently [A] is only partially available for quenching [D*]. Therefore $\boldsymbol{[D^*] \times k_R}$ in case II overestimates $\mathbf{RET_{D\to A}}$.

In case I (Figure 4-1) the acceptor population, [A], is initially completely unexcited and therefore, [A] is fully available to quench [D*] because the corresponding acceptor to *every* excited D molecule is unexcited and ready to receive an exciton. Hence, $RET_{D\to A} = [D^*] \times k_R$ accurately describes the instantaneous exciton transfer rate from D to A (i.e., $RET_{D\to A}$).

In case II (Figure 4-1) the A population has been excited before the excitation of the D population and as a result, some fraction of the D-A population cannot undergo RET because in that fraction, the donor and acceptor molecules are both simultaneously excited, rendering RET impossible, since no exciton can hop to an *excited* acceptor as long as it stays in the excited state. This makes the acceptor population only *partially* available for quenching [D*] and therefore $[D^*] \times k_R$ overestimates the instantaneous number of excitons transferred from [D*] to [A].

4.2.3 Networks with Exclusively-Excited Acceptors

A RET network is a supramolecular structure that holds multiple fluorophores at almost-fixed distances away from one another (e.g., fluorophores attached to a DNA grid). A population of such multi-fluorophore structures is represented by a graph (Figure 4-2) in which each node represents the *population* of one of the fluorophores of the corresponding structure. If all the acceptors in the network are fully available to their donors, Eq.4-1 can be extended to describe the decay of the excited-state population of every node in the network. For example, in Figure 4-2, assuming that a δ-pulse excites the M population, the decay of [N*] is accurately described by the following differential equation in which F, L and R are the rate constants of fluorescence, exciton loss, and RET, respectively.

$$\frac{d[N^*]}{dt} = -[N^*](F_N + L_N + R_{N\to P} + R_{N\to G}) + [M^*]R_{M\to N}$$

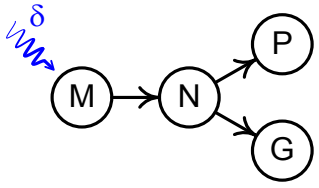

Figure 4-2 – Example of a RET network with exclusively-excited acceptors (RET directions shown by arrows) – For these networks an ODE system based on nominal RET-rate constants, accurately describes the decay of excited-state population of every node.

Full acceptor availability in RET networks is usually achieved when each node has only one source of excitation (e.g., either a single donor or a far-field source). Such networks can be accurately analyzed using the classical method according to which, an

ODE system based on *nominal* RET-rate constants (given by Eq.4-2), describes the kinetics of energy-migration in the network. For example, the complete ODE system for the RET network of Figure 4-2 is as follows:

$$\begin{cases} m' = -m(F_m + L_m + R_{m\to n}) + \delta(t)A(m) \\ n' = -n\left(F_n + L_n + R_{n\to p} + R_{n\to g}\right) + m \times R_{m\to n} \\ p' = -p\left(F_p + L_p\right) + n \times R_{n\to p} \\ g' = -g\left(F_g + L_g\right) + n \times R_{n\to g} \end{cases}$$

Where: $m \equiv [M^*]$; $m' \equiv \frac{d[M^*]}{dt}$; $F_m \equiv k_{F.M}$; $R_{m\to n} \equiv k_{R(M\to N)}$

4.2.4 Networks with Shared Acceptors

Förster's formula for calculation of RET-rate constants (Eq.4-2) assumes that the (unexcited) acceptor is only excited by a single donor, and hence is always available to receive an exciton from the donor. However, for acceptors with multiple excited donors (e.g. Z in Figure 4-3) this formula yields overestimated RET-rate constants because it ignores the partial unavailability of the acceptor induced by co-donors (i.e., fluorophores that share the same acceptor).

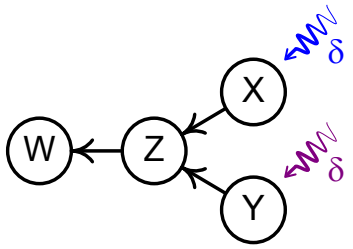

Figure 4-3 – Example of a RET network with a shared acceptor (arrows show RET directions) – For these networks the classical model (Eq.1) does NOT accurately describe the kinetics of energy migration in the network.

In a network of fluorophores, excitons might hop from one fluorophore to another as a result of RET. As illustrated in Figure 4-4, whenever multiple excitons (at different co-donors) simultaneously attempt to jump to the same unexcited acceptor, an *exciton race* occurs as a result of which, except for one exciton, all other transfers will be unsuccessful, because the acceptor molecule is excited by only a single exciton and therefore the rest of the excitons cannot successfully hop to the now-occupied (excited) acceptor[16].

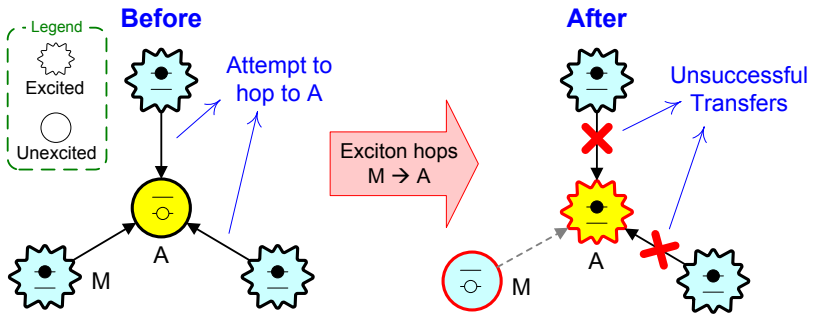

Figure 4-4 – Exciton race in a single 4-fluorophore structure: out of multiple simultaneously-competing excitons for the same unexcited acceptor molecule, only one exciton can hop to the acceptor and excite it, leaving other transfers unsuccessful.

Unsuccessful transfers cause the *effective* RET-rate constants to be lower than the *nominal* RET-rate constants which are calculated by Förster's formula. Therefore, for a network with an exciton race, the classical RET analysis method does not accurately describe the excited-state-population decay of the nodes. For example, nodes X and Y in Figure 4-3 are co-donors to node Z, and therefore, if [X*] and [Y*] are sufficiently high, Eq.4-1 based on $k_{R(X\rightarrow Z)}$ (Eq.4-2) cannot accurately describe the decay of [X*].

4.3 Mathematical Model of Partial Acceptor Saturation

Acceptor saturation is one of the forms of acceptor unavailability which is defined as the inability of an acceptor to receive an exciton from its excited donor. A number of factors can cause (partial) acceptor unavailability such as photo-bleaching, change in temperature, and the like; however, in this thesis for the sake of brevity, we only focus on two of these factors which cause acceptor saturation: 1-acceptor pre-excitation, and 2-exciton race, as these two factors, unlike others, cannot be easily controlled externally.

4.3.1 Modeling Acceptor Pre-excitation

As illustrated in Figure 4-1, acceptor pre-excitation occurs when the acceptor in a RET pair is excited before the donor, and stays excited sufficiently long such that for a period of time both of them are simultaneously in the excited state. We define the *ineffective population* (denoted by γ) to be the fraction of the excited donor population that has excited acceptors and consequently cannot undergo RET until their acceptors are de-excited. As shown in Figure 4-5, out of the two contributing factors to $RET_{D \rightarrow A}$ (i.e., [D*] and k_R), only [D*] is affected by acceptor pre-excitation; specifically, due to the absence of exciton race, the RET-rate constant remains unchanged, whereas [D*] is effectively reduced by γ.

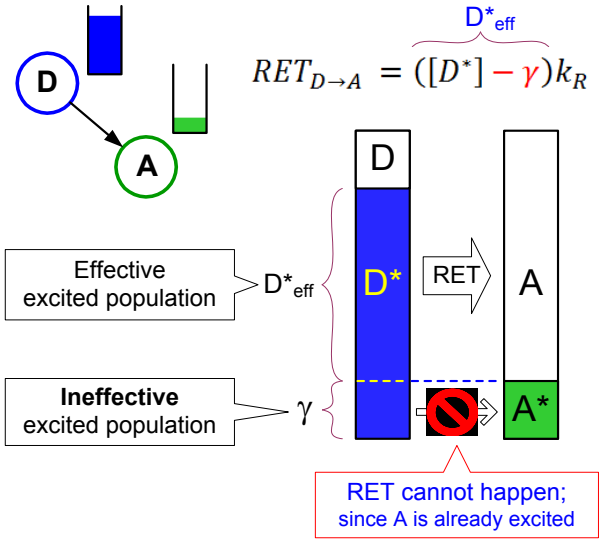

Figure 4-5 – Acceptor pre-excitation can be modeled as a reduction (γ) in the *effective* excited-donor population.

Therefore, in the absence of exciton race, the instantaneous rate of exciton transfer from D to A ($RET_{D\to A}$) under acceptor pre-excitation at any given time, can be obtained by subtracting the RET due to γ from the total RET due to [D*]. Hence, the decay of [D*] is accurately described by the following equation:

$$\frac{d[D^*]}{dt} = -[D^*](k_F + k_L) - \overbrace{([D^*] - \gamma)}^{[D^*]_{eff}} k_R$$

Unlike k_R (given by Eq.4-2) which is constant in the above equation, γ is not constant and changes in time, as [A*] undergoes de-excitation.

4.3.2 Modeling Exciton Race

Exciton race occurs when multiple simultaneously-excited co-donors compete for the same unexcited acceptor. As a result, some fraction of the excitons from each co-donor fails to hop to the acceptor (Figure 4-4) reducing its nominal pairwise RET to the

acceptor. This condition is illustrated in Figure 4-6 wherein D and B are simultaneously competing for A. In this example, the acceptor population is entirely unexcited, thus, we can assume that $[D^*]_{eff}=[D^*]$ for an infinitesimally short period of time ($\Delta t \to 0$). Therefore, out of the two contributing factors to $RET_{D\to A}$ (i.e., $[D^*]$ and k_R), only k_R is affected by exciton race; specifically, the reduction in $RET_{D\to A}$ due to exciton race, can be modeled as a reduction (β) in the *effective* RET-rate constant.

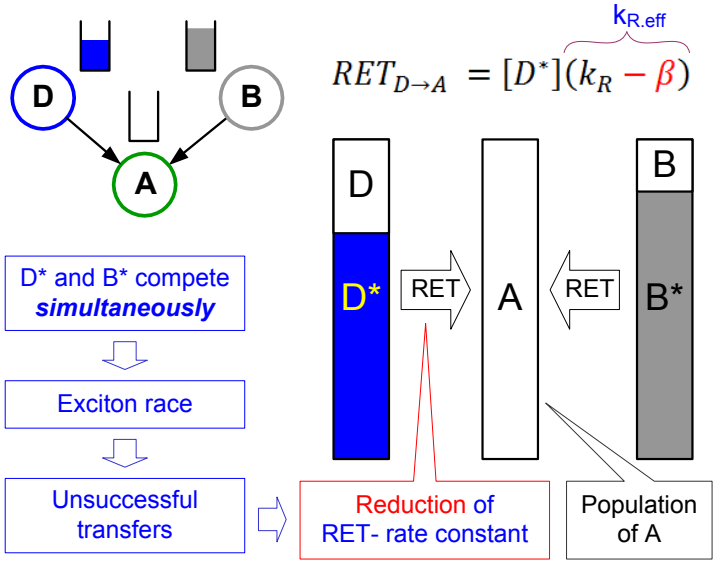

Figure 4-6 – Exciton race can be modeled as a reduction (β) in the *effective* RET-rate constant. kR is the nominal RET rate constant.

Hence, the decay of [D*] under exciton race (and in the absence of acceptor pre-excitation) can be accurately described by the following equation:

$$\frac{d[D^*]}{dt} = -[D^*](k_F + k_L) - [D^*]\overbrace{(k_R - \beta)}^{k_{R.eff}}$$

In the above equation, β is not necessarily constant and may change in time, as the excited population of the co-donors decay.

4.3.3 Decay Equations for Networks with Partial Acceptor Saturation

In general, partial acceptor saturation can be modeled as a reduction in either the effective excited population (Figure 4-5), or the effective RET-rate constant (Figure 4-6), or both. Hence, for a donor with a pre-excited acceptor under exciton race, the decay equation can be written in the following form (compare with Eq.4-1) wherein k_R is the nominal RET-rate constant:

$$\frac{d[D^*]}{dt} = -[D^*](k_F + k_L) - ([D^*] - \gamma)(k_R - \beta) \qquad (4\text{-}3)$$

Eq.4-3 is an *inhomogeneous* and *time-variant* differential equation because γ and β vary in time. A more general form of this equation which includes exciton migration to- and out of node N is given below, where $R_{N\to a}$ denotes the nominal rate constant of RET from N to a.

$$\begin{aligned}\frac{\mathrm{d}[N^*]}{\mathrm{d}t} &= -[N^*](k_F + k_L) \\ &- \sum_{a\in\{acceptors\ of\ N\}} ([N^*] - \gamma_{N\to a})(R_{N\to a} - \beta_{N\to a}) \\ &+ \sum_{d\in\{donors\ to\ N\}} ([d^*] - \gamma_{d\to N})(R_{d\to N} - \beta_{d\to N})\end{aligned} \qquad (4\text{-}4)$$

4.4 Karoon Algorithm

The kinetics of energy migration in a RET network with partially-saturated acceptors can be described by an ODE system composed of inhomogenous differential equations analogous to Eq.4-3 in which γ and β are time-varying terms. Since the closed-form formula for the $\gamma(t)$ and $\beta(t)$ terms is not known prior to solving the ODE (except for the simplest cases), existing numerical methods for solving inhomogenous ODE systems cannot be used to extract the desired kinetics in the system. Karoon is a domain-specific

algorithm for numerically solving such ODE systems based on a RET-specific method which calculates γ and β (see the supporting information).

4.4.1 Intuition

The principal idea that underlies Karoon is to incorporate acceptor saturation into RET calculations by partitioning the *effective* excited-donor population into several sections such that the donor-to-acceptor RET in each of them can be accurately described by a *single* effective RET-rate constant the value of which is fixed throughout the decay time. Specifically, in a RET pair (D→A) with a shared acceptor, the excitons hopping to A from the co-donors of D, render A less available to D, and consequently induce a reduction in the effective D-to-A-transfer efficiency. This reduction depends on the number of *excited* co-donors and their transfer likelihood, and as a result, different parts of the excited D-population, [D*], undergo RET to A with different *effective* rate constants. This is illustrated in Figure 4-7 in which nodes D, E and F are co-donors to node A, and [D*] is divided into four sections (denoted by ϑ) in each of which D is competing differently to excite A. For example, D in ϑ_4 is competing with one excited co-donor, whereas in ϑ_3 it is competing with two co-donors (E and F), and thus the effective RET-rate constant for the D-to-A transfer in section ϑ_3 (denoted by ξ_3) is less than that of ϑ_4 (i.e., $\xi_3 < \xi_4$). This means that a *single* rate constant (e.g., k_R) does not apply to the entire [D*], and consequently $RET_{D\to A} \neq [D^*] \times k_R$.

Karoon uses *multiple* (instead of only one) RET-rate constants to calculate the D-to-A exciton transfer. Specifically, based on the excitation status of the co-donors, [D*] is partitioned into several sections, each with a different effective RET-rate constant for $RET_{D\to A}$. For instance, $RET_{D\to A}$ in Figure 4-7, is described by partitioning [D*] into four sections ($[D^*] = \vartheta_1 + \vartheta_2 + \vartheta_3 + \vartheta_4$) because D has two co-donors; furthermore, in each section, $RET_{D\to A}$ has a different rate constant. As shown in this figure, ξ_1 is equal to k_R, which is the *nominal* rate constant for the D→A pair, because D in ϑ_1 is *the only* excited co-donor exclusively exciting A, whereas ξ in sections ϑ_2, ϑ_3 and ϑ_4, is only a *fraction* of k_R, since D in these sections is competing with other co-donors to excite A, and hence is less successful. Accordingly, the instantaneous value of $RET_{D\to A}$ is the sum of proportional contributions of all of these sections as summarized in the following equation in which ϑ_i denotes the instantaneous size of section *i*:

$$RET_{D\to A} = \sum_{i=1}^{4} \vartheta_i \xi_i = \vartheta_1\xi_1 + \vartheta_2\xi_2 + \vartheta_3\xi_3 + \vartheta_4\xi_4$$
$$= k_R \times (\vartheta_1 + \frac{\vartheta_2}{\sigma_2} + \frac{\vartheta_3}{\sigma_3} + \frac{\vartheta_4}{\sigma_4})$$

The key advantage of this method over MCS is that the σ_i values can be directly calculated from nominal RET-rate constants, leading to the significantly-higher speed of Karoon. Specifically, Monte-Carlo methods require a sufficiently-large sample set, the collection of which typically involves millions of iterations, whereas, the σ_i values in Karoon (Figure 4-7) are calculated using a novel method that we have developed which does not rely on any statistical sampling.

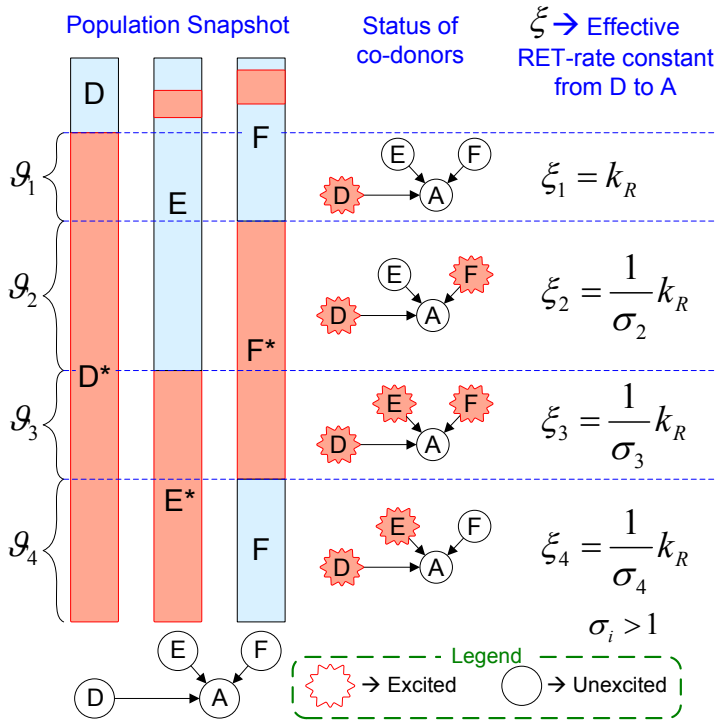

Figure 4-7 – Excited donor population, [D*], is divided into four sections, in three of which ξ (effective rate constant) is only a fraction of k_R. The σ_i values are calculated without statistical sampling. Here, $\sigma_i > 1$, $i \in \{2,3,4\}$ thus $0 < \xi_3 < \xi_{2,4} < \xi_1$

4.4.2 Algorithm Outline

Similar to classical numerical methods, the simulation time in Karoon is divided into many short intervals (Δt), called *time steps*, during each of which the system is assumed to be linear, i.e., the de-excitation rates are assumed to be constant. With this assumption and starting from a set of initial conditions, the algorithm obtains the system status in each time step based on its status in the previous time step, until the system status in all the time steps is extracted. The system status is the instantaneous size of excited population for every node.

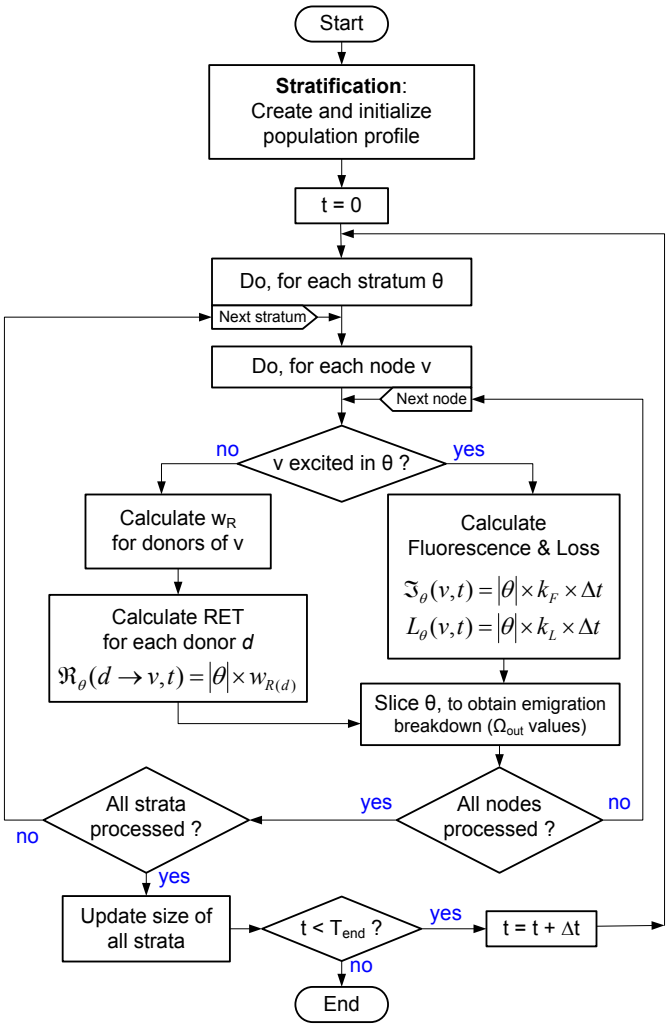

Figure 4-8 – Overview of Karoon

As illustrated in Figure 4-8, Karoon starts with population *stratification*, which is a special partitioning (explained later) of the sample population into a fixed number of sections each called a *stratum*. The response of each stratum (e.g., fluorescence, RET, etc.) is usually different from that of the other strata because the set of *effective* RET-rate constants, which describes the given network, varies across these strata. Moreover, the overall response of the network is proportionally generated by all of the strata, the

contribution of each of which is weighted by its size. Strata sizes are stored in a vector called the *population-profile* vector which maintains the latest distribution of the sample population among the strata. The change in this distribution – which is caused by excitation and de-excitation of nodes – is modeled as inter-stratum population migration.

In each time step, every stratum is processed *independently* to obtain its response as well as its population migration to other strata. After all the strata are processed, the migration data are used to update the population profile to be used in the next time step, and finally the simulation time is advanced by Δt. This cycle is repeated until the simulation time reaches the end of simulation (T_{end}).

The time evolution of fluorescence, RET, and exciton-loss is obtained using the following formulae, wherein w denotes the weight of the corresponding de-excitation process (explained later), and θ_i^t is the size of stratum i at time t, and E(D) is the set of strata in which D is excited:

$$\mathfrak{F}(D,t) = \sum_{i \in E(D)} \theta_i^t \times w_{F(D)} \qquad (4\text{-}5)$$

$$\mathcal{L}(D,t) = \sum_{i \in E(D)} \theta_i^t \times w_{L(D)} \qquad (4\text{-}6)$$

$$\mathcal{R}(D \to A,t) = \sum_{i \in E(D)} \theta_i^t \times w_{R(i,D \to A)} \qquad (4\text{-}7)$$

4.4.3 Population Stratification

For the excitation status of a single fluorophore we consider two possible states: the *excited* and *unexcited* states, denoted by 1 and 0 respectively. Similarly, for a multi-

fluorophore structure the excitation status is a vector each component of which uniquely represents the excitation status of one of the fluorophores in the structure. Therefore, for an *n*-fluorophore structure, a total of 2^n states are possible. For example, in a population of single RET pairs (2-fluorophore structures) at any given time each pair can be in one of the four possible states (i.e., 00, 01, 10 and 11).

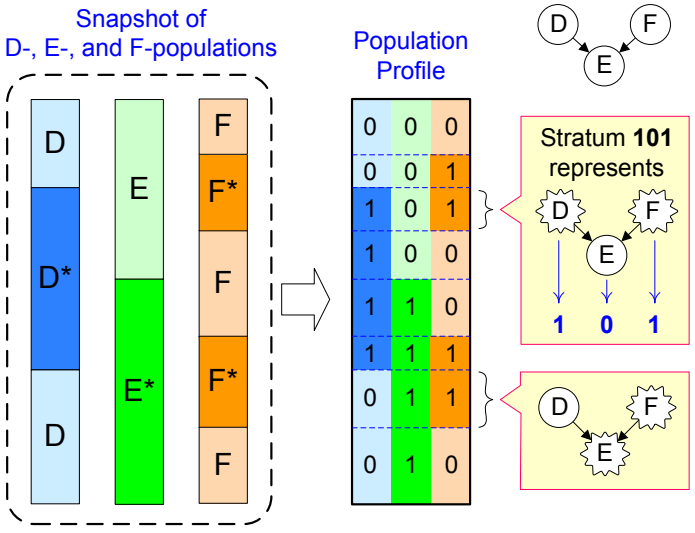

Figure 4-9 – Population stratification in Karoon – Here, the population profile has eight strata each representing a subset of the total population; e.g., stratum 011 represents <D, E*, F*> (structures with excited E and F).

The population of multi-fluorophore structures in Karoon is represented by a set of strata each of which corresponds to one of the possible excitation states. Specifically, a stratum is the collection of all structures in the population which have the same excitation status; for example in Figure 4-9, stratum *101* represents the collection of all structures in which D and F are excited and E is unexcited, i.e., <D*, E, F*>. In this

example, since there are three fluorophores in each supramolecular structure, a total of eight strata can represent the entire population at any time.

Each stratum, at any given time, has a share of the total population (denoted by θ), which due to the de-/excitation of fluorophores, varies in time. The *population profile* is the set of all these shares, therefore:

$$total\ population\ size = \sum_{i=1}^{2^n} \theta_i$$

4.4.4 Inter-stratum Population Migration

As the excitation status of fluorophores changes over time, the population composition of each stratum also undergoes modification; for instance in Figure 4-10 – which shows the population-profile evolution for an example network – during every time step ($\Delta t \to 0$) some fraction of the *001*-population turns to *000* because fluorophore *G* de-excites (through fluorescence and exciton loss). This change is modeled as a population migration from stratum 001 to stratum 000.

Inter-stratum population migration changes the population distribution among the strata (Figure 4-10), and since the most recent distribution is required in each time step, the population-profile vector is updated based on the size of migrating populations from each stratum to other strata. Specifically, the population profile is updated at the end of each time step, according to the following formula wherein θ_i^{t+1} denotes the population-size of stratum *i* at time *t+1*:

$$\theta_i^{t+1} = \theta_i^t + \underbrace{\sum_{q=1}^{s} \Omega_{q\to i}^t}_{Entering} - \underbrace{\sum_{q=1}^{s} \Omega_{i\to q}^t}_{Leaving}$$

In the above equation, s is the total number of strata, and $\Omega_{q\to i}^t$ denotes the subpopulation of stratum q that migrates to stratum i during time step t.

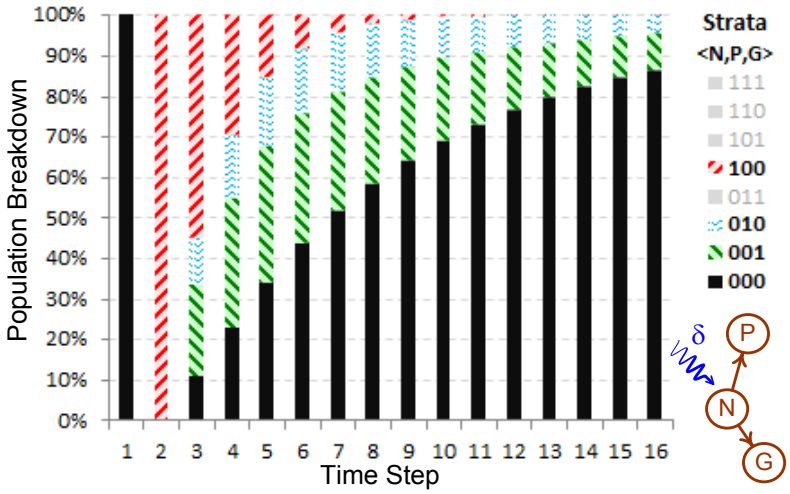

Figure 4-10 – Evolution of the population profile for an example network – Initially the entire population is unexcited, and hence, in stratum 000. At the second time step, a delta pulse excites all N fluorophores causing the population to migrate to stratum 100. In the subsequent time steps the population gradually migrates (de-excites) back to 000, either directly or through other strata (010 and 001).

The breakdown of outbound migration (Ω_{out} values) for each stratum is obtained by successively partitioning (or *slicing*) its population using *migration vectors* which represent excitation or de-excitation pathways. Specifically, every factor that changes the excitation status of the stratum population (photon absorption, fluorescence, RET, etc.) is represented by a migration vector (denoted by <w,t>) which has two components: 1-*weight*, which determines the fraction of the stratum population that is affected by the

vector, and 2- *target*, which specifies the affected node(s). Each stratum has its own set of migration vectors which determine the destination and size of its migrating sub-populations (i.e., *slices*). Specifically, each migration vector proportionally splits a slice into two *new* slices, one of which corresponds to a new destination stratum. For instance, Figure 4-11 illustrates the breakdown of population migration out of stratum 011 in an example network with a single donor (D) and two acceptors (A and F). Here, three migration vectors are applicable to stratum 011: <0.2, D>, <0.3, F>, and <0.5, D→A> which represent the fluorescence of D and F, and RET from D to A, respectively (exciton loss is ignored). The partitioning starts with the first vector, which – by modifying 20% of the stratum (weight=0.2) – divides it into two slices. Likewise, the second vector creates two more slices. The third vector affects two of the four existing slices and therefore, its weight (i.e., 50%) is proportionally distributed between them, creating a total of six slices. Figure 4-11 shows that in each time step, only 21% of the population of stratum 011 remains in this stratum, and that the rest of its population migrates to five other strata 000, 001, 010, 100, and 101 at the following rates respectively: 6%, 14%, 9%, 15%, and 35%. Furthermore, since F in this stratum is excited, the D→F RET vector is ignored, because RET to an excited acceptor is not possible (See the supporting information for more details).

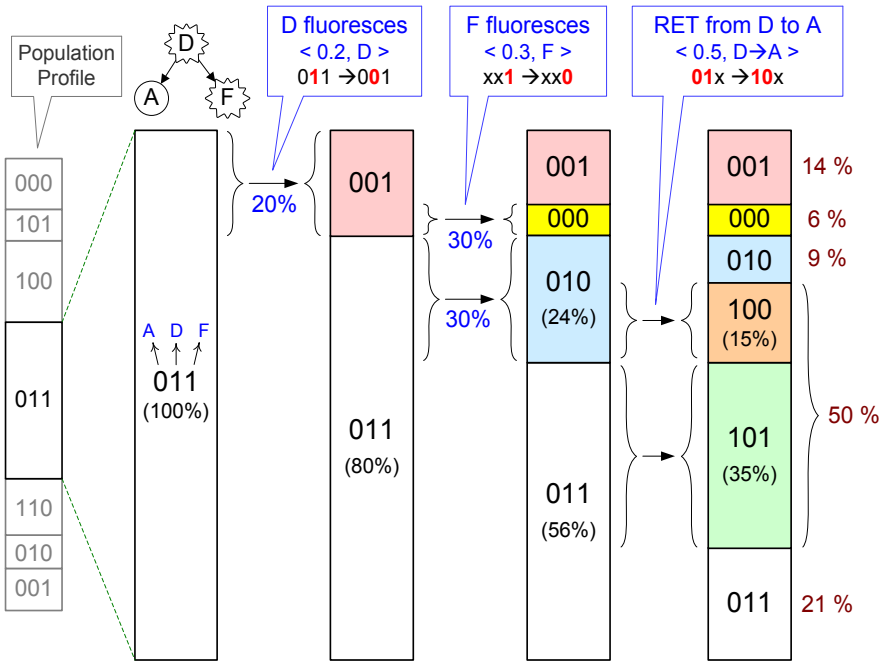

Figure 4-11 – Stratum slicing, to extract breakdown of population migration out of stratum 011 in an example network – Three migration vectors <0.2, D>, <0.3, F>, and <0.5, D→A>, slice the 011-population into six slices, each corresponding to a destination stratum; e.g., 35% of the 011-population migrates to the 101 stratum.

4.4.5 Calculation of Migration Weights

As mentioned before, migration weights – which specify the fraction of the stratum population affected by corresponding migration vectors – are used to obtain the size of slices (i.e., migrating populations out of a stratum) as well as the stratum response. The calculation of these weights depends on the nature of the physical phenomenon associated with them (photon absorption, chemical reaction, fluorescence, etc.). In this section, the fluorescence, loss and RET weights are derived, and in the supporting information, the weight of far-field excitation is derived from Beer's law.

4.4.5.1 Loss and Fluorescence Weights

Fluorescence weights can be derived by decomposing Eq.4-3 into three de-excitation components. Specifically, based on Eq. 3 we can write:

$$\frac{\Delta[D^*]}{\Delta t} = -[D^*](k_F + k_L) - ([D^*] - \gamma)(k_R - \beta)$$

Multiplying the above equation by Δt yields the following equation in which $\mathfrak{F}$, $\mathcal{L}$, and $\mathcal{R}$ denote the change in the excited-state population during Δt due to fluorescence, exciton loss and RET, respectively.

$$\Delta[D^*] = -\Delta t \times \left([D^*](k_F + k_L) + ([D^*] - \gamma)(k_R - \beta)\right)$$

$$= -\underbrace{\Delta t \times [D^*] \times k_F}_{\mathfrak{F}(D^*)} - \underbrace{\Delta t \times [D^*] \times k_L}_{\mathcal{L}(D^*)} - \underbrace{\Delta t \times RET}_{\mathcal{R}(D^*)}$$

This implies $\mathfrak{F}(D^*) = [D^*] \times \Delta t \times k_F$ and thus, the fluorescence weight, i.e., the fraction of [D*] that fluoresces during each time step, is $w_F = \Delta t \times k_F$. Similarly, the migration vector for exciton loss can be shown to have a weight of $w_L = \Delta t \times k_L$. Since k_F and k_L are both unaffected by exciton race, the fluorescence- and loss migration vectors are unchanged across different strata.

4.4.5.2 RET Weights

RET weights in each stratum are calculated by accounting for the mutual effects of the competition among *active* RET pairs on one another. This implies that, in each stratum, *inactive* RET pairs are excluded from RET weight calculations. A RET pair is considered active, only when its donor is excited, and its acceptor is unexcited. In Figure 4-12 for example, W→Z in stratum 1010, and Y→Z in stratum 0011 are both

inactive and excluded from weight calculations, for different reasons: unexcited *donor* population for W→Z, and entirely excited *acceptor* population for Y→Z.

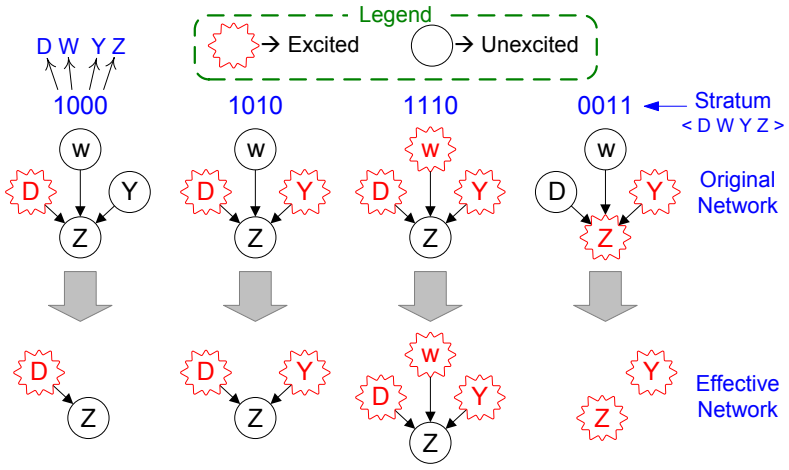

Figure 4-12 – Equivalent effective network corresponding to a selection of strata – Inactive RET pairs are excluded from weight calculations.

Every *active* RET pair in a stratum is associated with a unique migration vector, the weight of which depends on the race condition at its *acceptor*: if the acceptor is not under any exciton race, then $w_R = \Delta t \times k_R$, otherwise, w_R is determined by *collision resolution* which is our method for calculating each co-donor's share of a common acceptor. Specifically, this method involves an *acceptor-centric* arbitration step which calculates the percentage of successful exciton transfers from each co-donor, and thereby its effective RET-rate constant to the shared acceptor. To further clarify this method, next we calculate w_R for the D→Z pair in every stratum of Figure 4-12 assuming that $k_{R(D\to Z)} = 4$, $k_{R(W\to Z)} = 8$, $k_{R(Y\to Z)} = 7$, and Δt=0.1.

Starting from stratum 0011, all w_R values are zero because none of the RET pairs in this stratum are active. In stratum 1000, since D→Z is the only active RET pair, the population of node D is the only entirely-excited donor population, *exclusively* exciting the acceptor (Z) without any exciton race, and hence, the nominal RET-rate constant $k_{R(D\to Z)}$ can accurately describe the decay of [D*] in this stratum. Therefore, $\mathcal{R}(D \to Z) = [D^*_{1000}] \times \Delta t \times k_{R(D\to Z)}$ and thereby $w_{R(D\to Z)} = \Delta t \times k_{R(D\to Z)}$.

Unlike in stratum 1000, the population of node D in stratum 1010 is competing with the Y-population for exciting Z, causing exciton race at Z which means that in some fraction of the 1010-population, excitons from D and Y simultaneously (with respect to a non-zero Δt) attempt to hop to Z as a result of which some fail to hop, because an unexcited Z molecule only accepts a single exciton (not two). Therefore, since multiple active donors (D and Y) are competing for the same acceptor, the calculation of RET weights for this stratum involves an extra step (called *arbitration*) to determine the fraction of *successful* exciton-hops from each donor. Explicitly, since Z in stratum 1010 has two *active* donors (D and Y), its population undergoes a total of four different competition scenarios which are denoted by $\bar{D}\bar{Y}, \bar{D}Y, D\bar{Y}, and\ DY$; for instance, $\bar{D}Y$ represents the fraction of the population in which excitons only from Y (and *not* from D) attempt to hop to Z during Δt. Each of these scenarios yields a different hopping-success rate for different co-donors; therefore, in order to obtain RET weights, each scenario is *arbitrated* (Ψ) and then *weighted* by its occurrence probability (P) according to Eq.4-8 wherein *d* and

a denote the donor and the (unexcited) acceptor, respectively, and *H(d)* is the set of all scenarios in which excitons from *d* attempt to hop to *a*.

$$w_{R(d\to a)} = \sum_{s \in H(d)} P(s) \times \Psi(s) \qquad (4\text{-}8)$$

P(s) is calculated from the nominal RET-rate constants of the *active* donors in scenario *s*. Specifically, the probability that an exciton *attempts* to hop to an acceptor, depends on the transfer efficiency to that acceptor; for instance, in stratum 1000, $w_{R(D\to Z)}$ is the fraction of excitons at D that hop to Z during Δt, this means that an exciton at D *attempts* to hop to Z during Δt with a probability of $P(D) = \frac{[D^*_{1000}]\times\Delta t\times k_{R(D\to Z)}}{[D^*_{1000}]} = \Delta t \times k_{R(D\to Z)}$ where $[D^*_{1000}]$ denotes the population of stratum 1000. By definition, the probability that an exciton at D does *not* attempt to hop to Z is $P(\bar{D}) = 1 - \Delta t \times k_{R(D\to Z)}$. Moreover, since excitons at D and Y *independently* attempt to hop to Z, we can write $P(DY) = P(D) \times P(Y)$; in this fashion, as illustrated in Figure 4-13, the probability of all different scenarios can be calculated from the nominal RET-rate constants according to the following equations wherein $\check{D} = \Delta t \times k_{R(D\to Z)}$ and $\check{Y} = \Delta t \times k_{R(Y\to Z)}$.

$$P(DY) = P(D) \times P(Y) = \check{D} \times \check{Y}$$
$$P(D\bar{Y}) = P(D) \times P(\bar{Y}) = \check{D} \times (1 - \check{Y})$$
$$P(\bar{D}Y) = P(\bar{D}) \times P(Y) = (1 - \check{D}) \times \check{Y}$$
$$P(\bar{D}\bar{Y}) = P(\bar{D}) \times P(\bar{Y}) = (1 - \check{D}) \times (1 - \check{Y})$$

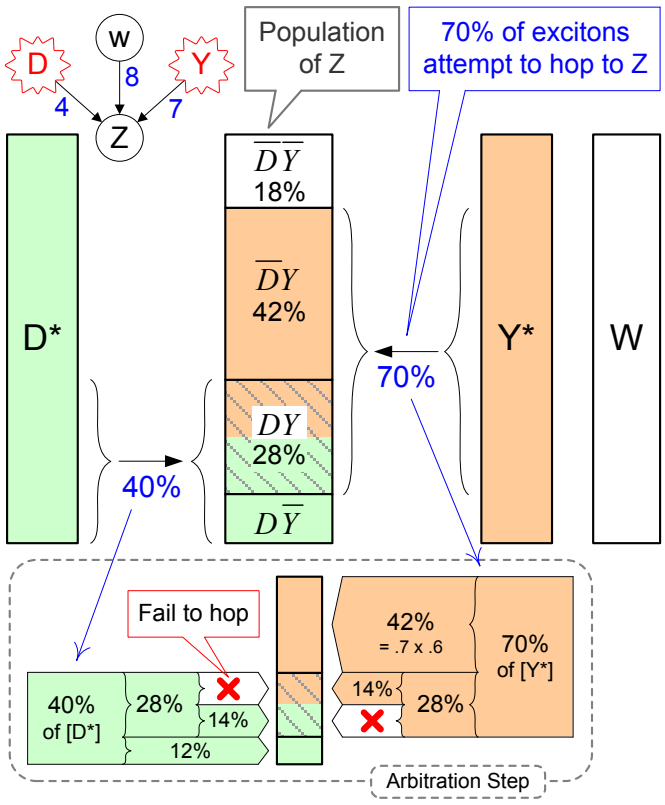

Figure 4-13 – Occurrence probability of each possible competition scenario in stratum 1010 – nominal RET-rate constants are: $k_{R(D\to Z)} = 4$, $k_{R(Y\to Z)} = 7$, and Δt = 0.1; thus, the hopping-attempt probabilities are 0.4 and 0.7 respectively – Exciton race occurs in 28% (0.4×0.7) of the Z population and since Ψ(DY) = 50%, only half of these excitons can successfully hop.

Ψ(s) in Eq.4-8 denotes the arbitration result of scenario s which determines the fraction of *successful* attempts by each donor in this scenario. In this thesis, we assume that acceptors do not prefer any particular donor, and thus, if n co-donor populations *equally* attempt to excite an acceptor population, each of them wins an equal share of $\frac{1}{n}$ of the acceptor population. This assumption leads to an arbitration model which we call the *indiscriminant-acceptor* model according to which, for a population of acceptors with n excited donors, if the exciton at *every* donor molecule attempts to hop to the acceptor

during Δt, only $\frac{1}{n}$ of each donor's attempts will be successful because, not preferring any particular donor, every acceptor molecule *randomly* accepts one out of the n exciton-offers that it receives during $\Delta t \approx 0$, making the success probability *equal* for all of its donors. In Figure 4-13 for example, $P(DY) = 28\%$ which implies that in 28% of the 1010-population, both D and Y attempt to hop to Z during Δt and since each Z molecule only accepts a single exciton, the success rate in this scenario is 50% which is denoted by $\Psi(DY) = \frac{1}{2}$.

Intuitively, $\Psi(\bar{D}Y) = \Psi(D\bar{Y}) = 1$, because in both these scenarios (i.e., $\bar{D}Y$ *and* $D\bar{Y}$) only a single donor is attempting to send excitons to the acceptor which causes no exciton race, and consequently, all the attempts are successful. It should be noted that, as a result of stratification, all the excited donors in each stratum have equal population sizes and consequently all active co-donors *in each competition scenario* – even if they have different transfer efficiencies to the common acceptor – attempt to send *equal* number of excitons to the acceptor, making the "$\frac{1}{n}$" arbitration rule applicable to all scenarios. Nevertheless, without loss of generality, any other application-specific arbitration model can also be used to calculate the success rates in each scenario.

Based on this discussion, in stratum 1010 (Figure 4-12) $H(D) = \{DY, D\bar{Y}\}$ and the weight of D→Z is calculated using Eq.4-8, as follows:

$$w_{R(D\to Z)} = P(DY) \times \Psi(DY) + P(D\bar{Y}) \times \Psi(D\bar{Y}) = P(DY) \times 0.5 + P(D\bar{Y}) \times 1$$
$$= P(D)\left(0.5P(Y) + \left(1 - P(Y)\right)\right) = P(D)\left(1 - 0.5P(Y)\right)$$
$$= \Delta t \times k_{R(D\to Z)}\left(1 - 0.5 \times \Delta t \times k_{R(Y\to Z)}\right)$$

Since D in all of the scenarios of H(D) is attempting to hop, we can rewrite P and Ψ as $P(s) = P(D) \times P(\tilde{s})$, and $\Psi(s) = \frac{1}{1+\varphi(\tilde{s})}$ wherein $\tilde{s}$ denotes the modified version of scenario s in which D is removed. Thus, Eq.4-8 can be also written in the form of Eq.4-9 in which $\varphi(\tilde{s})$ is the number of co-donors in $\tilde{s}$ that are attempting to hop to a.

$$w_{R(d\to a)} = \underbrace{\Delta t \times k_{R(d\to a)}}_{P(d)} \times \sum_{\tilde{s}\in H(d)} \frac{P(\tilde{s})}{1+\varphi(\tilde{s})} \qquad (4\text{-}9)$$

Collision resolution is performed on a *per-acceptor* basis and can be summarized in a table which we call the SiCES map (/ˋsaIsɛs/) which stands for Simultaneous Competition of Excitation Sources. As shown in Table 4-1, each row in a SiCES map corresponds to a different competition scenario.

Table 4-1 – SiCES map for Z in stratum 1010 of Figure 4-13

s	P	Ψ		(P × Ψ) Successful hops to Z: from D	from Y
$\bar{D}\bar{Y}$	18 %	-		0	0
$\bar{D}Y$	42 %	1		0	42 %
$D\bar{Y}$	12 %	1		12 %	0
DY	28 %	½		14 %	14 %
100 %			Σ	26 %	56 %
				$w_{R(D\to Z)}$	$w_{R(Y\to Z)}$

As the last example, the RET weight calculation for stratum 1110 (Figure 4-12) is detailed in the SiCES map of Table 4-2. In this stratum, D is competing with two other co-donors (W and Y) for exciting Z and since the acceptor in this stratum has three active donors, a total of eight competition scenarios can occur which are listed in the SiCES map.

As mentioned earlier, the weight of the same RET pair usually differs in different strata, as its acceptor undergoes different race conditions; in Figure 4-12 for instance, the weight of the D→Z pair in stratum 1000, 1010 and 1110 is 40%, 26% and 17.47%, respectively. The reduction in $w_{R(D\to Z)}$ is due to the competition of D with other co-donors to excite Z. This reduction also indicates that, as expected, the increase in the exciton-race rate at Z, reduces the effective RET from D to Z.

Table 4-2 – SiCES map for Z in stratum 1110 of Figure 4-13

s	P	Ψ		(P × Ψ) Successful hops to Z: from D	from W	from Y
$\bar{D}\bar{W}\bar{Y}$	3.6 %	-		0	0	0
$\bar{D}\bar{W}Y$	8.4 %	1		0	0	8.4 %
$\bar{D}W\bar{Y}$	14.4 %	1		0	14.4 %	0
$\bar{D}WY$	33.6 %	½		0	16.8 %	16.8 %
$D\bar{W}\bar{Y}$	2.4 %	1		2.4 %	0	0
$D\bar{W}Y$	5.6 %	½		2.8 %	0	2.8 %
$DW\bar{Y}$	9.6 %	½		4.8 %	4.8 %	0
DWY	22.4 %	1/3		7.47 %	7.47 %	7.47 %
	100 %		Σ	17.47 %	43.47 %	35.47 %
				$w_{R(D\to Z)}$	$w_{R(W\to Z)}$	$w_{R(Y\to Z)}$

4.5 Validation

In this section we mathematically validate some parts of our algorithm. Additionally, we report the simulation results of two saturated networks, and demonstrate that Karoon captures the intuitively-expected saturation effects. And finally, we quantitatively validate Karoon with experimentally-supported data reported in the literature, as well as by comparing it against MCS results.

4.5.1 Mathematical Validation

Karoon is expected to be equivalent to the classical RET-analysis method (Eq.4-1), in two general cases: first, for de-excitation processes that are not affected by saturation, and second, in the absence of saturation. Here, we mathematically prove these two cases.

4.5.1.1 Kinetics of fluorescence and exciton loss

Since the rate constant of fluorescence is not affected by partial saturation of nodes, the kinetics of fluorescence described by Karoon (Eq.4-5) should match that of Eq.4-1. To show this, we first rewrite Eq.4-1 using Δt:

$$\frac{-\Delta[D^*]}{\Delta t} = \underbrace{[D^*] \times k_{F(D)}}_{Fluorescnce} + \underbrace{[D^*] \times k_{L(D)}}_{Loss} + \underbrace{[D^*] \times \Sigma k_{R(D \to A)}}_{RET} \qquad (4\text{-}10)$$

The fluorescence contribution to Δ[D*] at time t in Karoon is denoted by $\mathfrak{F}(D,t)$ and is given by Eq.4-5 wherein E(D) is the set of those strata in which D is excited; therefore, the combined size of them yields [D*], i.e., the instantaneous size of the excited-D population, and hence, $\sum_{\theta_i \in E(D)} \theta_i^t = [D^*]$:

$$\mathfrak{F}(D,t) = \sum_{\theta_i \in E(D)} \theta_i^t \times w_{F(D)} = \underbrace{w_{F(D)}}_{k_{F(D)} \times \Delta t} \times \underbrace{\sum_{\theta_i \in E(D)} \theta_i^t}_{[D^*]}$$

$$= [D^*] \times k_{F(D)} \times \Delta t$$

Where θ_i^t denotes the size of stratum i at time t. The above equation shows that the calculation of $\mathfrak{F}(D,t)$ in Karoon yields the same result as that of Eq.4-1.

In the same fashion (using k_L instead of k_F), we can show that the kinetics of exciton loss described by Karoon is exactly equivalent to the one described by Eq.4-1.

4.5.1.2 Absence of Saturation

In the absence of saturation, Karoon should be equivalent to the classical method for describing the kinetics of energy migration in multi-fluorophore networks (i.e., a system of ODE's similar to Eq.4-1). To show this, it is sufficient to prove that whenever saturation effects are negligible, Eq.4-7 in Karoon is equivalent to the RET component of Eq.4-10. The other two components of Eq.4-10 (i.e., fluorescence and loss) were shown above to be the same as those of Karoon (Eq.4-5 and Eq.4-6).

Absence of saturation in a network has two implications: First, in each RET pair, the donor and the acceptor can never both be excited, simultaneously; thus, $[D^*]_{eff} = [D^*]$ holds for every RET pair in the network. The second implication is that the co-donors of a shared acceptor cannot be *simultaneously* excited. Under these conditions, if D in stratum *i* is *excited*, all its acceptors and its co-donors must be *unexcited* (otherwise $\theta_i=0$) which implies that every acceptor in each stratum is exclusively excited by no more than one *active* donor, leading to a competition-free excitation scenario for that donor. Therefore, according to Eq.4-9, for any RET pair (D→A) if D is excited in stratum *i*, then $w_{R(i,D\to A)} = \Delta t \times k_{R(D\to A)}$ based on which Eq.4-7 can be rewritten as follows:

$$\mathcal{R}(D \to A, t) = \sum_{i=1}^{S} \theta_i^t \times w_{R(i,D\to A)} = \Delta t \times k_{R(D\to A)} \times \underbrace{\sum_{i\in E(D)} \theta_i^t}_{[D^*]_{eff}}$$

$$= \Delta t \times k_{R(D\to A)} \times [D^*]_{eff}$$

By writing the above equation for *all* of the acceptors of D, we obtain $\mathcal{R}(D \rightarrow \Sigma A, t) = \Delta t \times [D^*] \times \Sigma k_{R(D \rightarrow A)}$ which is equivalent to the RET component of Eq.4-10, proving that the classical method is a special case of Karoon, in the absence of saturation.

4.5.2 Qualitative Validation

The effects of partial saturation on the RET-network response often cannot be captured by the classical RET analysis method. To qualitatively verify that Karoon can capture these effects, we designed two experiments and compared the results with the classical method.

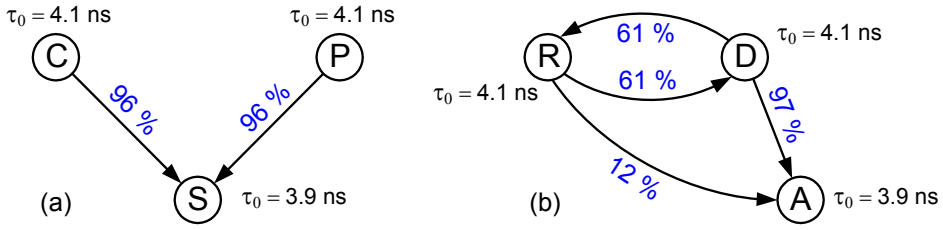

Figure 4-14 – RET networks used for qualitative validation of Karoon – The number on each arrow indicates the corresponding transfer efficiency.

4.5.2.1 Congested Acceptor

The RET network of the first experiment (Figure 4-14.a) is composed of an acceptor (S) that is shared by two competing co-donors (C and P). Further, the transfer rates are noticeably greater than the de-excitation rates (k_L+k_F) of the acceptor, causing it to appear as a congested exciton sink. A δ-pulse, at time t=0, excites over 95% of [C] and [P], after which [S] is populated by excitons coming from [C*] and [P*].

Intuitively, [S*] is expected to be capped by ||S||, i.e., the total number of S molecules in the sample; however, since the classical method is oblivious of the population size, as shown in Figure 4-15, it predicts [S*] to exceed ||S||, which is impossible. Karoon, on the other hand, predicts [S*] to be always less than ||S||, which qualitatively indicates that this algorithm is capturing saturation effects.

4.5.2.2 Re-excited Donor

In the second experiment (Figure 4-14.b), two identical donors share the same acceptor, but one of them (D) has a higher transfer rate to the acceptor than the other. Initially, the entire donor populations ([D] and [R]) are excited by a δ-pulse, after which we expect to see a *peak, preceded by a dip*, in [D*]. This is because, due to saturation, the mutual transfer between D and R is initially negligible; however, as [D*] declines faster than [R*], after a while, the R→D path becomes unblocked, and R starts to re-excite D, causing the peak after the dip in [D*].

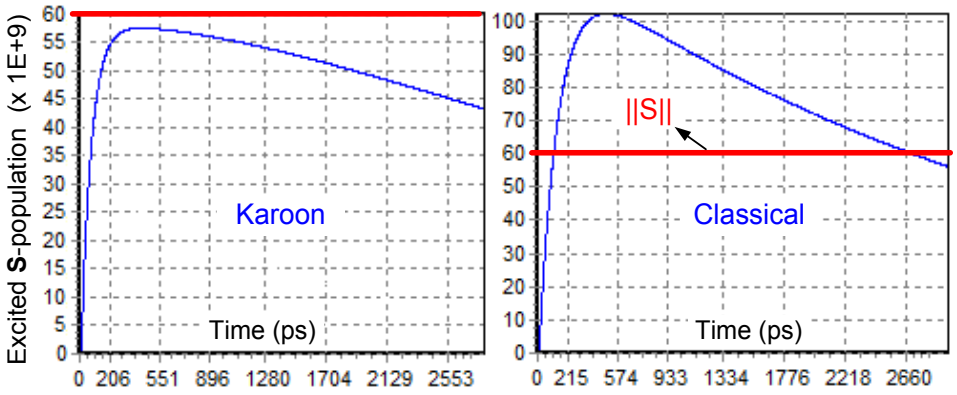

Figure 4-15 – [S*] as a function of time, simulated with Karoon and classical method – In the results of the classical method [S*] exceeds ||S||, which cannot happen in reality.

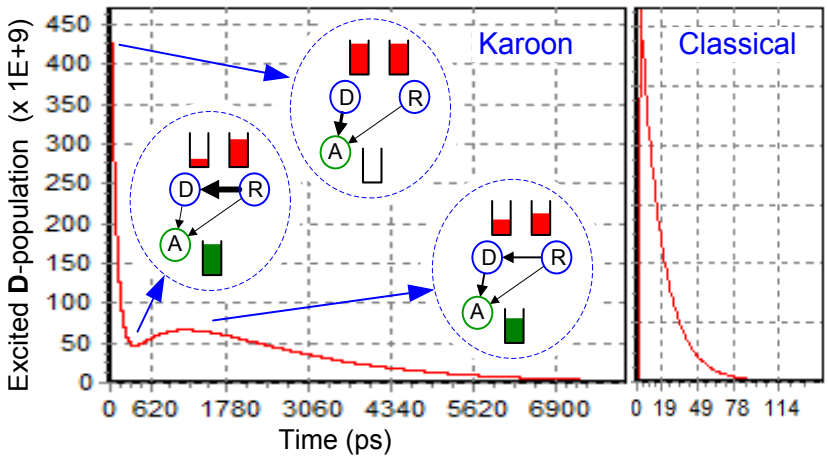

Figure 4-16 – [D*] as a function of time, simulated with Karoon and classical method (Figure 4-14.b) – Unlike Karoon, the classical method does not capture the repopulation of [D] by [R*].

As shown in Figure 4-16, the classical method cannot capture the saturation effect, because, being oblivious of the population size, the classical method never sees the D→A path blocked due to saturation, therefore, excitons hopping from [R*] to [D] continue to be *quickly* drawn by [A], leaving no chance for the R→D path to dominate the D→A path. This example is a demonstration of a saturation effect captured by Karoon.

4.5.3 Quantitative Validation

To further validate our algorithm, we used Karoon to simulate several RET networks the responses of which were available to us from other sources. Specifically, Watrob[23] et al. have provided theoretical analysis supported by experimental data for three different RET networks. We simulated these three networks with Karoon, and confirmed that its results were perfectly consistent with their results within the

numerical error range (due to $\Delta t \neq 0$). The details of this comparison are reported in the supporting information. Additionally, we compared Karoon with Monte-Carlo RET simulation (detailed in the next section and the supporting information), and verified that they both yield consistent results for the same RET network, and same excitation conditions.

4.6 Evaluation and Discussion

To evaluate the performance of Karoon, we simulated (simulation length=8000ps, and Δt=1ps) several RET networks with Karoon and also with a typical Monte-Carlo-based RET-simulation (MCS) algorithm[17, 20, 24] and compared the results in terms of precision and simulation speed. Both simulation algorithms were implemented using C++ and were compiled with the same compiler and run on the same machine (64-bit Intel Core-i5 at 2.3 GHz). For details about the simulated RET networks, see the supporting information.

While the numerical error in both MCS and Karoon depends on time resolution (i.e., Δt), the quality of results in MCS is additionally affected by the simulation precision. Specifically, being a deterministic method, Karoon always yields the same result for the same input, whereas the stochastic nature of MCS causes variability in the results of repeated simulations of the same input. The precision of a Monte-Carlo method is proportional to $\sigma/\sqrt{N}$ in which σ is the standard deviation of the underlying population and N is the number of observed events[21]. This indicates that after *quadrupling N*, only

a *two*-fold precision improvement can be achieved. Consequently, as shown in Figure 4-17, depending on the network, only after (tens or hundreds of) millions of cycles, does the precision in MCS, approach that of Karoon. It should be noted that, the number of iterations in MCS is usually more than N because in many iterations, excitons do not hop and thereby N remains unchanged.

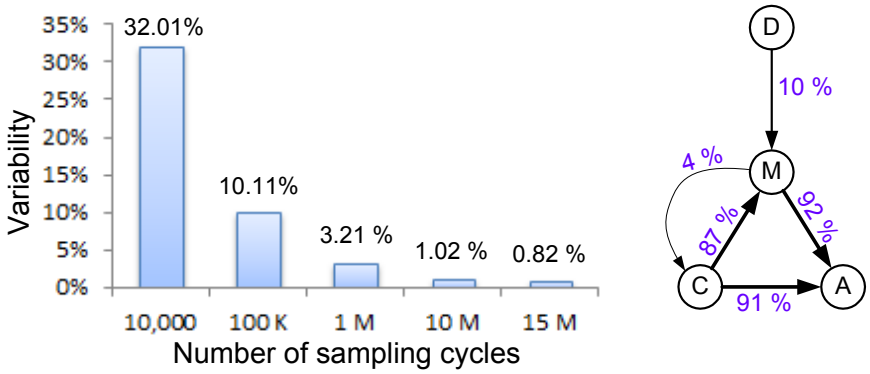

Figure 4-17 – Variability in MCS results: only after 15 million iterations, does the MCS precision approach that of Karoon (i.e., no variability). The simulated network is shown on the right.

The latency of Karoon is compared in Figure 4-18 with that of the MCS (with 15 million iterations) for different sizes of RET networks. As seen in the figure, depending on the network size, Karoon is several orders of magnitude faster than MCS. For instance, the latency of simulating a 4-node network with Karoon is 530ms, whereas MCS takes ~147 hours to simulate the same network, showing that Karoon is ~one million times faster than MCS, for that network.

4.6.1 Why is Karoon faster?

The faster simulation in Karoon is because in each time step, it requires noticeably fewer calculation cycles compared with Monte-Carlo methods; for example, while MCS

requires millions of sampling cycles per time step to simulate a 4-node network, Karoon requires only 16 calculation cycles per time step (as there are only 2^4=16 strata). This significant speedup is achieved at the cost of limited scalability; specifically, the population-profile vector in Karoon grows exponentially with the number of nodes in the network. Despite this limitation, Karoon still enables a fast, precise and reliable analysis tool for most applications of RET as they often involve analyzing relatively small networks (i.e., n < 25). For larger networks divide-and-conquer approaches (or the like) should be used.

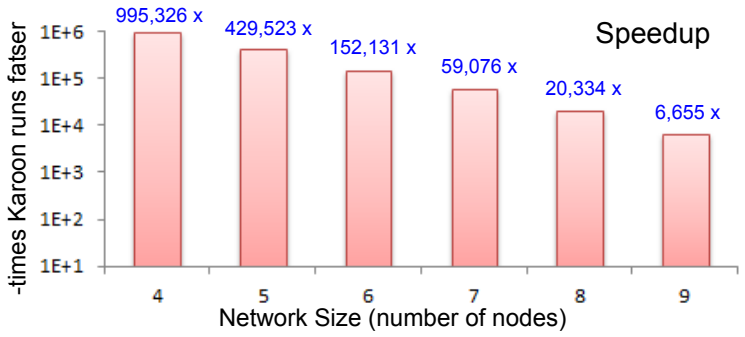

Figure 4-18 – Speedup: Karoon is several orders of magnitude faster than MCS.

4.6.2 Future work

In this thesis, for the sake of brevity we ignored a number of RET-related phenomena many of which can be easily incorporated into Karoon. For instance, exciton annihilation mechanisms can be modeled by modifying the collision-resolution procedure. Photo-bleaching can be modeled by a second profile vector which permanently (or temporarily) disables excitation pathways for the bleached population. We leave the details of these models for future work.

4.7 Summary and Conclusion

First-order kinetics fails to accurately describe exciton migration in a multi-donor multi-acceptor network, wherein the pre-excitation of acceptors, and exciton race cause RET-rate constants to effectively change in time, and hence not to be *constant*. To address this issue, we augmented the classical rate equations with two time-varying terms to account for exciton race and pre-excitation, to thereby enable a more accurate description of energy migration in saturated networks based on *inhomogeneous time-variant* ODE systems. Further, we introduced a numerical algorithm, called Karoon to solve such time-varying ODE systems.

Karoon splits the network population into a fixed number of strata, each one of which – proportional to its size – contributes to the overall network response. Moreover, throughout the simulation, it keeps track of inter-stratum population migration, to weight the instantaneous contribution of each stratum to the overall network response. Unlike the classical method which describes each RET pair by only a *single* rate constant, Karoon uses *multiple* possibly-different rate constants (one for every stratum) to describe a RET pair. Calculation of these rate constants is enabled by the population homogeneity of the strata, as the entire population of each stratum is in the same excitation state.

Our evaluations show that Karoon is orders of magnitude faster and more precise than MCS, which makes it suitable for throughput-sensitive applications of FRET, such as FRET microscopy and RET-circuit design.

5 Thousand-fold increase in optical storage density by polychromatic address multiplexing

In this chapter we demonstrate how FRET circuits can be used to improve the areal density of optical storage devices. The proposed density-enhancement solution is based on a FRET-enabled multiplexing technique, called PAM, which can be used in other domains and applications, as well. In later chapters, we will demonstrate how PAM can be useful in FRET microscopy.

5.1 Introduction

The demand for high-density digital storage is increasingly growing in the age of digital media for a variety of reasons including archival purposes and smaller sizes required in mobile devices. Optical storage techniques are among the oldest and most commonly employed to tackle this issue. Higher storage density in mainstream reflective media (such as DVD and Blu-Ray) is achieved by increasing the density of pits, i.e., small depressions on a DVD surface, used to store data. However, the pit (cell) density of optical media is constrained by the diffraction limit that imposes a classical spatial resolution of approximately $\lambda/2$, where λ is the wavelength of light used to interrogate the media [25]. Thus, optical storage density can only be linearly improved, in the classical limit, by reducing the wavelength of light and is practically more limited by the availability of laser sources and reflective, or photoactive media in that band. Many techniques have been investigated to solve this problem [26-32], among which increasing the bit density of each cell is particularly promising for its potential to

increase storage density, even at low cell densities, by introducing a new recording dimension. In this regard, due to their unique properties, DNA-based methods have been extensively used to achieve higher structural densities.

Here, we demonstrate a novel retrieval technique which we call polychromatic address multiplexing (PAM) to access multiple bits stored in the same cell. By exploiting nanoscale fluorescence-based storage elements, PAM enables storage of hundreds of bits in a single cell. In this fashion, higher storage densities beyond the diffraction limit are achieved with this technique which can also be incorporated into conventional optical-storage technologies.

5.2 PAM-Disc Structure

A conceptual schematic of a PAM disc is illustrated in Figure 5-1. A PAM disc can have several physical layers of storage. Each physical layer consists of many spatially resolved cells each of which contains a large number of storage elements enabling storage of many bits per cell. A *word* is a collection of bits in a cell associated with a single address and a *word address* is a unique combination of incident excitation colors (wavelengths) e.g., generated by an integrated LED or laser array, which activates the subset of storage elements in the cell that collectively store the word value corresponding to that address. Consequently, the activated storage elements cause a fluorescence increase which is eventually translated to the binary value of the addressed word.

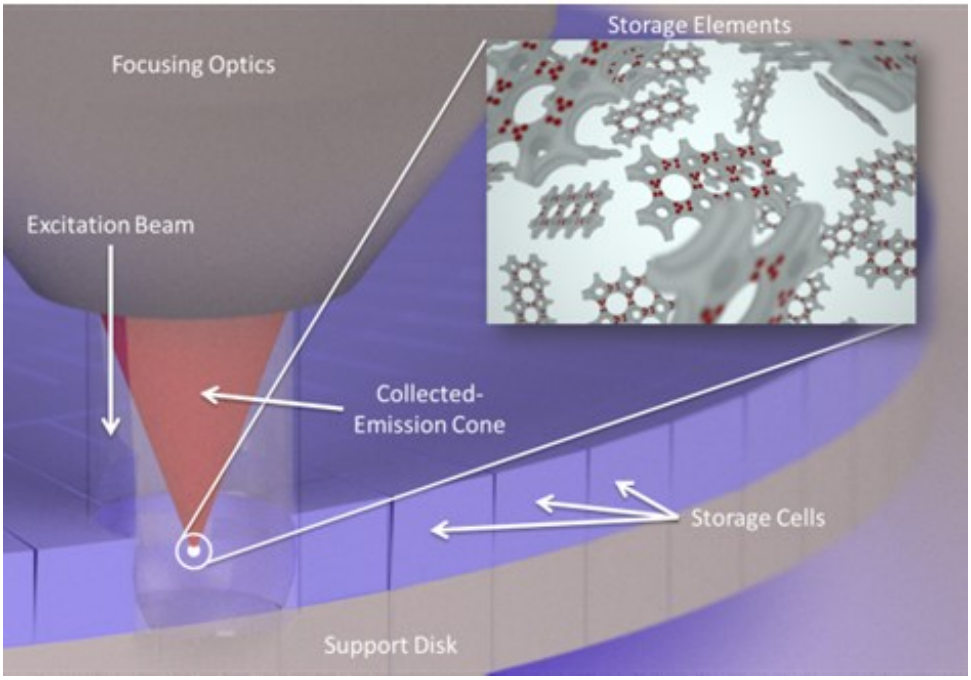

Figure 5-1: PAM disc structure: a large number of cells packed on a surface, each of which containing a large number of storage elements.

The storage element in PAM, which we call a PEPE (photo-erasable PAM element), operates based on Förster Resonance Energy Transfer (FRET) and is composed of a set of fluorophores placed on a grid-like DNA nanostructure. The simplest form of a PEPE, which is called an ER-PEPE, (illustrated in Figure 5-2) is a UV-disruptable FRET-pair in which the donor and acceptor molecules (E and R) act as the Excitation port and Read port, respectively. The R molecule is attached to the DNA substrate via a photo-cleavable linker [33]. Upon UV irradiation the E-R pair is disrupted, since the linker is irreversibly cleaved and therefore R diffuses away (or the dipole-dipole alignment between E and R is reduced) to eliminate RET entirely, consequently reducing the

fluorescence of R, I_R. In this manner a logical binary value can be stored and retrieved by measuring the change in acceptor fluorescence (ΔI_R) and discriminating against two possible levels.

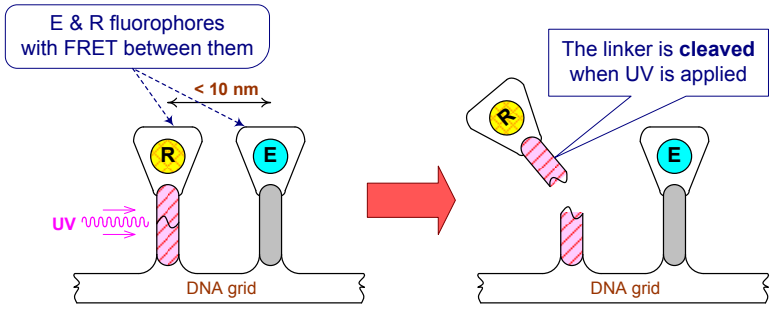

Figure 5-2: Structure of the basic storage element, an ER-PEPE, before and after writing

5.3 Polychromatic Address Multiplexing

With ER-PEPEs we can only store a single bit in each cell which does not yield densities beyond the diffraction limit. To further increase the storage density of cells, we investigated storing several words in different channels in the same cell each of which has a unique address. A channel is a collection of PEPEs that are activated with the same address.

The logical equivalent of PAM is illustrated in Figure 5-3. In each cell, multiple channels exist all of which are normally inactive. When an address is applied to the cell, only the corresponding channel is activated and contributes to an increase in the read-out signal which is eventually interpreted as the binary value of the word at that address.

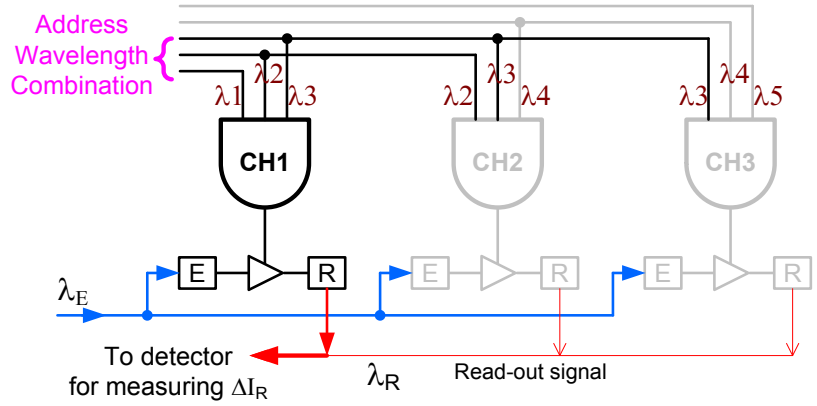

Figure 5-3: logical equivalent of PAM: only the addressed channel contributes to the output while others remain inactive.

To enable addressing, we augment the ER-PEPE with a set of acceptors, i.e., the address vector, which strongly quench the E and R as shown in Figure 5-4. Depending on its address vector, each PEPE in a cell belongs to a certain channel. Channel selection in PAM is based on *acceptor saturation* (satFRET) [3] which is a method for reversibly reducing the effective transfer efficiency in a FRET pair by directly exciting the acceptor and hence making it less available for quenching the donor.

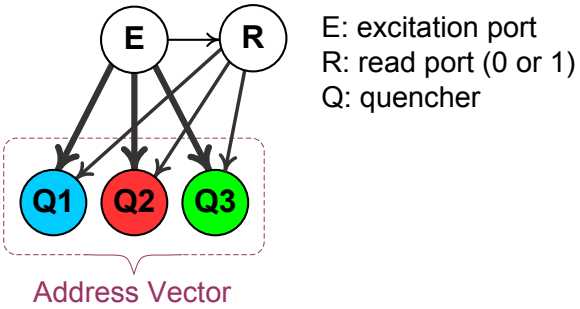

Figure 5-4: ER-PEPE is augmented with a set of quenchers

Figure 5-5 illustrates channel selection in PAM: When E is excited by λ_E, in the absence of any addressing wavelength (Figure 5-5b) most of the excitons generated at E

are absorbed by the address vector because the address-vector acceptors strongly quench E and R and consequently R exhibits weak fluorescence. However, E and R cannot be efficiently quenched by the address vector when it is saturated (Figure 5-5a) by the incident wavelengths of the address beam, leading to an increase in the fluorescence of R. This increase (ΔI_R) is only caused by the addressed PEPEs since all others are strongly quenched by their unsaturated address-vector acceptors. If the addressed PEPEs have missing R's (due to a write operation) the ΔI_R value will be near zero which implies a logical zero. A ΔI_R value above some threshold indicates intact E-R pairs on the addressed PEPEs which can be interpreted as logical one.

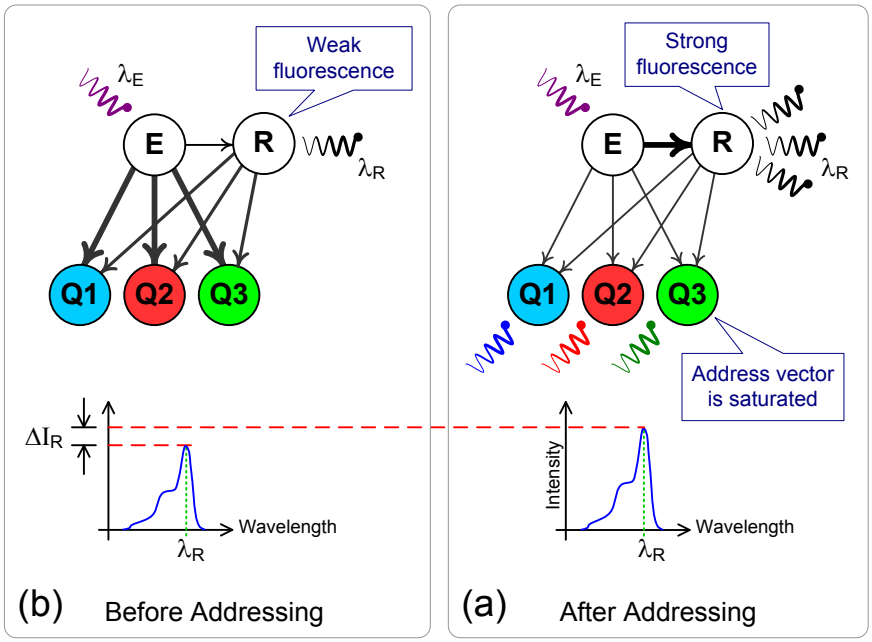

Figure 5-5: An augmented PEPE before and after being addressed: fluorescence of R increases.

5.3.1 Multilevel PAM

By enabling several channels in the same cell, PAM increases the storage density. It can also be coupled with other techniques to further increase the storage density. For example, we can incorporate multilevel decoding into PAM to increase channel capacities. The resulting technique yields multi-bit channels which enable the storage of multiple bits per address (i.e., wider words in each channel).

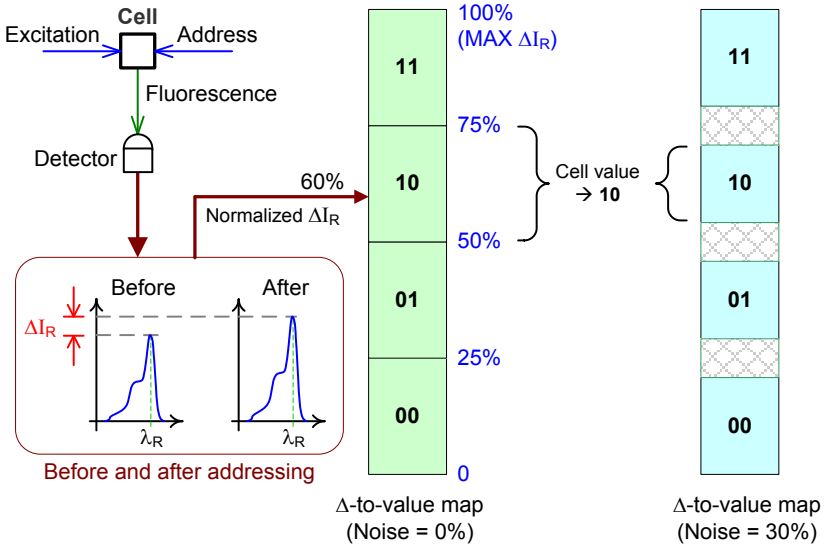

Figure 5-6: Multilevel decoding uses multiple thresholds for value mapping – Noise limits maximum allowed levels – Encoding two bits requires four ΔI_R levels (thresholds).

As shown in Figure 5-6, in this method the ΔI_R of a channel is not compared with only a single level (threshold); instead, multiple thresholds define several intervals, each of which correspond to a unique multiple-bit binary value and the value stored in the channel corresponds to the interval within which the normalized ΔI_R falls. For example in Figure 5-6, the value of the channel is '10' because the normalized ΔI_R (i.e., 60%) lies

within the interval (50%, 75%). A ΔI_R-to-value map is used in this technique which defines 2^n normalized thresholds for n-bit channels. Before being compared against the map, the ΔI_R of each channel is normalized to its $\Delta I_{R\text{-}Max}$ which is the increase in fluorescence due to the addressed channel when all E-R pairs of the channel are intact.

5.3.2 Write Operation

The write operation happens only once (write-once-read-many storage) and is performed by dissociating E-R pairs. Initially each channel has a large number of PEPEs with intact E-R pairs (yielding $\Delta I_{R\text{-}Max}$). The write operation in multilevel PAM involves dissociating only a fraction of the population of E-R pairs in the channel (as opposed to the regular PAM in which the *entire* E-R population is dissociated); for example in Figure 5-6, dissociating 40% of the pairs has reduced ΔI_R from 100% (i.e., $\Delta I_{R\text{-}Max}$) to 60%. Partial dissociation can be achieved by controlling the duration of UV-irradiation, however, the specific fraction cannot be selectively addressed by UV light, i.e., the photo-cleavable linker is non-specifically excited by <350 nm photons. It may be possible to enable selective dissociation of PEPEs by exciting the photo-cleavable linker through a selectively quenched exciton wire [34], similar to PAM, instead of by direct UV illumination, however, we leave this for future work.

5.4 Evaluation

In this section we first experimentally demonstrate a storage cell with a single-bit address line (monochromatic address) after which we detail the simulation of a storage cell with multi-bit address (polychromatic address).

5.4.1 Monochromatic Channels

5.4.1.1 Experimental Demonstration

We experimentally demonstrated the proof-of-principle for single-bit PAM channels, multilevel decoding and multi-bit PAM channels the results of which are reported in this section. We used self-assembled DNA-based PEPEs in our experiments. To design uniquely addressable PEPEs we developed a custom spectral analysis program that, given the spectra and photophysical properties of ~300 commercially available dyes and stains[4], searches for as many optimal collections of fluorophores as possible according to criteria such as emission-peak separation, spectral overlap, minimal direct excitation, etc.. We constrained the specific geometry of the PEPEs to reflect our best knowledge of the microenvironment and spatial coordinates at the distal ends of the DNA tiles we used [2, 35]. By this method we evaluated ~250,000 candidate designs for single-bit PEPEs (Figure 5-7a) out of which 210 satisfied our criteria.

[4] ATTO-Dyes (www.atto-tec.com) and Alexa-Fluor Dyes (www.invitrogen.com)

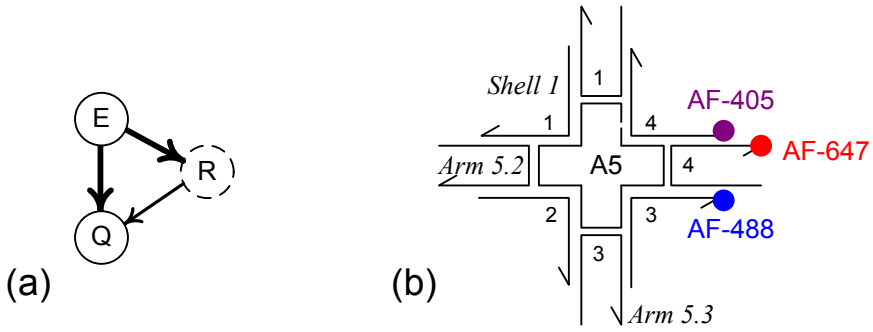

Figure 5-7: RET network for the PEPEs used in our experiments (a), Structure of a DNA-based PEPE (b)

From our initial design search we chemically synthesized two kinds of PEPEs, ERQ_{TR} and ERQ_{647}, each composed of three fluorophores (see Figure 5-7b): AlexaFluor-405 (AF405) as the excitation port (E), AlexaFluor-488 (AF488) as the read port (R), and an address port (Q) of either TexasRed (TR) or AlexaFluor-647 (AF647) for ERQ_{TR} and ERQ_{647}, respectively. The E fluorophore is excited by 405nm wavelength light and resonantly transfers energy to the R and Q fluorophores. The intensity of fluorescence at the emission peak of R (λ_R=520nm) is recorded as a function of the saturation of Q (by either λ_{Q1}=660nm or λ_{Q2}=592nm) due to direct excitation which causes an increase in the fluorescence of R.

To demonstrate single-bit PAM channels, we prepared four memory cells, each with equal molar concentrations of channel1- and channel2-PEPEs, to statically store each possible two-bit combination. The results of this experiment are shown in Figure 5-8. To store a logical 0 we used EQ-PEPEs, which have no R in their RET network, emulating a fully dissociated channel. All two-bit binary combinations were composed from mixtures of (EQ- or $ERQ-)_{647}$ and (EQ- or $ERQ-)_{TR}$; for example, to store

the binary value '10' we mixed ERQ_{647} with EQ_{TR}. Since each channel can be independently read, each stored binary value is distinguishable from the other channel, as shown in Figure 5-8. We detected a worst-case crosstalk of 20% between channels which is due to slight spectral overlap between the excitation of TR and AF647. In this experiment, the two single-bit channels are in the same cell which yields a total capacity of two bits per cell.

We also created ER_q PEPE's to ascertain that the observed ΔI_R was solely caused by (partial) saturation of Q. In these PEPE's the Q fluorophore was placed far enough away from E and R such the E→Q and R→Q transfer efficiencies were negligible and as expected ΔI_R was measured to be close to zero for cells with ER_q PEPE's.

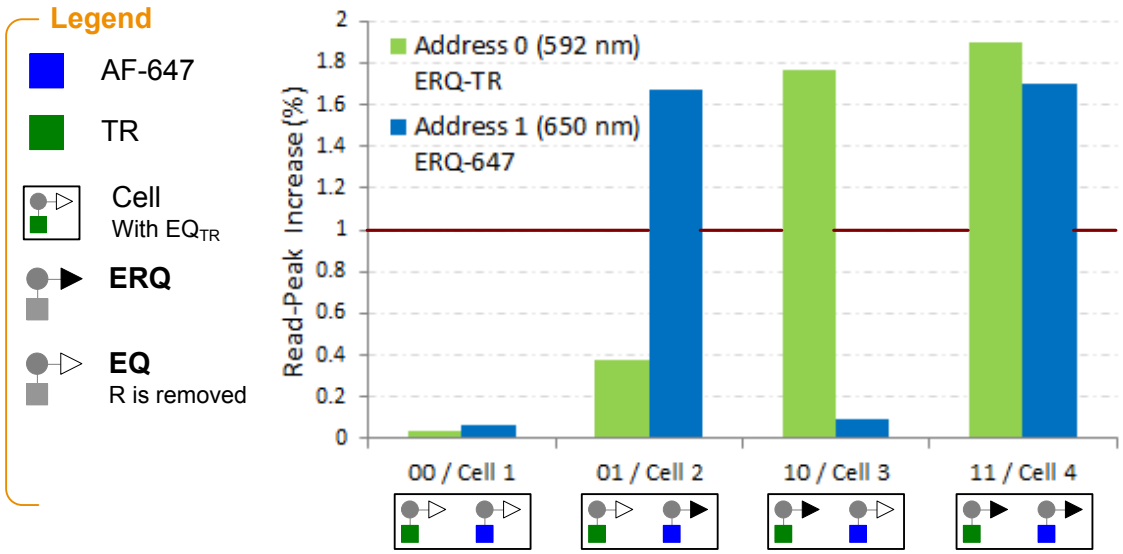

Figure 5-8: Single-bit PAM channels: four cells storing four different 2-bit values (each cell: two channels, 1-bit words) – total cell capacity: 2 bits

To demonstrate the compatibility of our storage elements (PEPEs) with multilevel encoding/decoding, we reduced the normalized ΔI_R of the channels by

separately exposing them to successive 15- to 20-second doses of UV light. As shown in Figure 5-9 we were able to write eight code words into each channel and successfully retrieve them. We started with two fully-intact channels in two separate cells to represent the '111' binary values. Every UV dose partially dissociated the E-R pairs in each channel and reduced the normalized ΔI_R of the channel by ~12% which was sufficient to change the interpreted value of the channel. In this manner we step-by-step changed the value of each channel from 111 to 000, one bit at a time. Due to the noise in our experimental setup we were not able to distinguish more than eight levels for each channel. In this experiment each 3-bit channel is in a separate cell yielding a total capacity of three bits per cell. As shown in Figure 2-9, the inter-molecular distance for freely diffusing molecules at concentrations < 50μM is greater than 20nm which implies that the freed (cleaved) R chromophores cannot parasitically contribute to the signal. This fact was also experimentally verified in Figure 5-9.

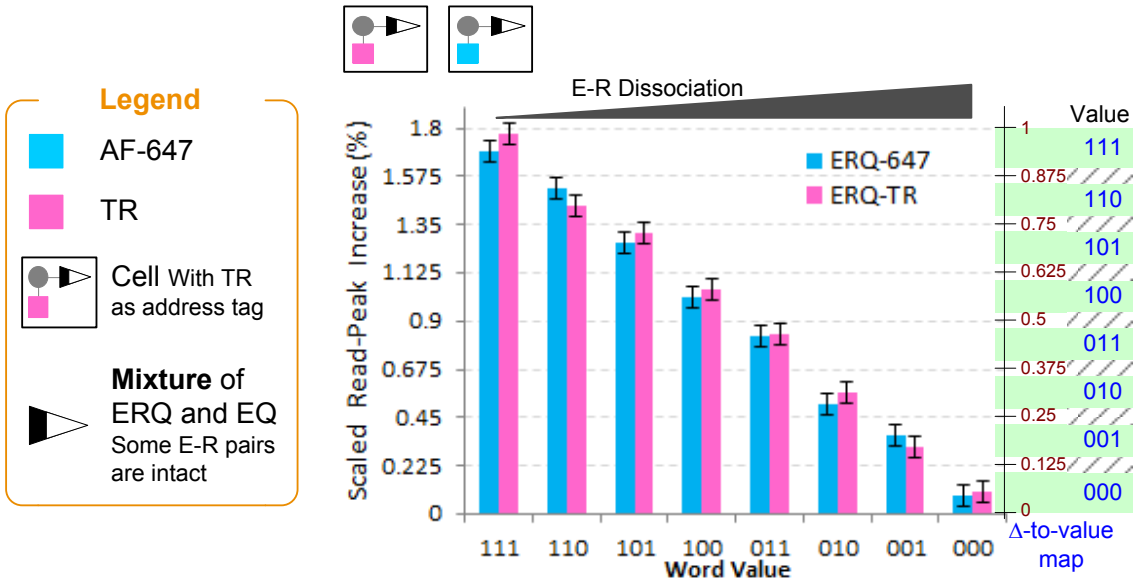

Figure 5-9: Multilevel Decoding: two channels in separate cells (each cell: one channel, 3-bit words) – total cell capacity: 3 bits

According to Figure 2-8, the observation of steady-state FRET at a low concentration (< 50nM) is a proof that the donor and acceptor molecules are held close to each other by some mechanism other than diffusion. Furthermore, we can also conclude that free R chromophores (cleaved after the write operation) at low concentrations, cannot form parasitic FRET pairs (after they diffuse away) to contribute to the read-out signal.

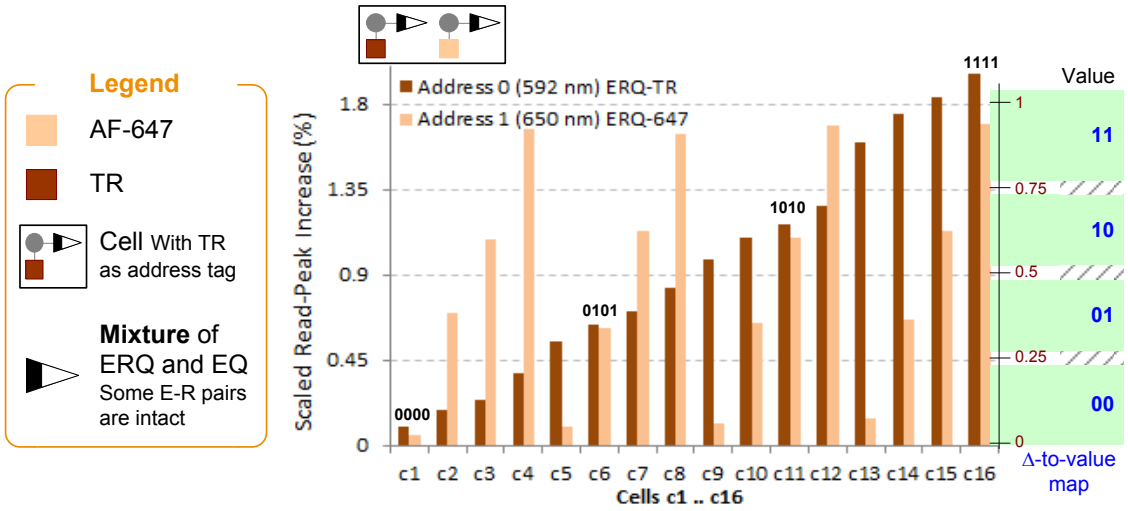

Figure 5-10: Double-bit PAM channels: 16 cells storing different 4-bit values (each cell: two channels, 2-bit words) – total cell capacity: 4 bits

As a demonstration for multi-bit PAM channels we mixed two channels with different dissociation levels into the same cell, to obtain a storage cell with two double-bit channels. And as shown in Figure 5-10 we could successfully store and retrieve all 16 possible binary values. Although separately, up to eight levels could be resolved for each channel (Figure 5-9), due to the 20% crosstalk between the two channels, only four levels could be used for encoding data when the two channels were in the *same* cell. Arbitrary dissociation levels were achieved by varying the mixing ratio of EQ- with ERQ-PEPEs for each channel. In this experiment, both double-bit channels are in the same cell, yielding a total capacity of four bits per cell.

5.4.1.1.1 Calculation of ΔI_R

ΔI_R is the change in the fluorescence intensity of the R fluorophore due to the saturation of the address tag. To measure ΔI_R we compared the output spectra (from the spectrometer) before and after saturation, over a window of wavelengths around λ_R;

specifically, we calculated the area under the fluorescence curve before and after saturation for interval [λ_R-α, λ_R+α] and then calculated the difference: $\Delta I_R = S_{after} - S_{before}$. A low-intensity violet LED was used as the common excitation port source (λ_E=405±10nm) and two high-intensity LED's as address sources (λ_{A1}=660±10nm, λ_{A2}=592±10nm). In the figure below the integration window is shown as well as three different curves: 1- The base curve (when no tag is addressed), 2- The TR-curve, which is when TexasRed is addressed, and 3- The 647-curve, which is when AF-647 is addressed.

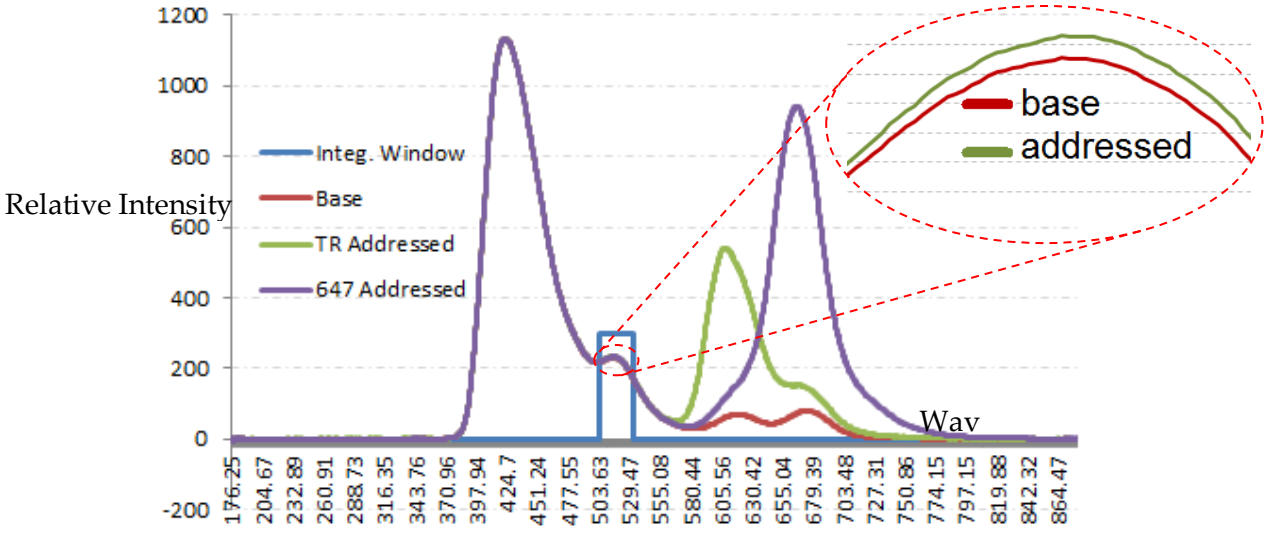

Figure 5-11: ΔI_R calculation: the difference in the area under the curve in the specified integration window is calculated before and after address-tag saturation – four peaks here (from left to right): fluorescence peak of the E and R fluorophores, and address tags (AF–647 and TexasRed)

For the double-channel-cell experiment, 16 different cells were prepared with 16 different combinations of channel values (00.00 through 11.11). The value stored in a channel can be changed by changing its ΔI_R. Removing the address tag from the PEPEs in a channel creates EQ-PEPEs (vs. ERQ-PEPEs) and decreases the ΔI_R of the channel.

Therefore, the value of a channel is determined by the concentration ratio of EQ- to ERQ-PEPEs; in our experiment, a channel with all EQ-PEPEs stores the value of 00, while a channel with all ERQ-PEPEs stores the binary value of 11. Effectively, when a 11-valued channel is diluted with EQ-PEPEs, its value changes to 10, 01 and finally 00, depending on the dilution level. To overcome cell-to-cell variations, ΔI_R values are normalized to $\Delta I_{R\text{-}MAX}$ which is generated by the cell with no EQ-PEPEs. The concentration of each channel is reported in Table 5-1.

Table 5-1 – Concentration of ERQ-PEPE's used in the experiments

Cell	Binary Value		Concentration (nM)		Number of ERQ-PEPEs	
	Channel 1	Channel 2	Channel 1 TR	Channel 2 647	ERQ-TR (Channel 1)	ERQ-647 (Channel 2)
Cell 1	00	00	15	50	2.26E+11	7.53E+11
Cell 2	00	01	15	195	2.26E+11	2.94E+12
Cell 3	00	10	15	330	2.26E+11	4.97E+12
Cell 4	00	11	15	500	2.26E+11	7.53E+12
Cell 5	01	00	140	50	2.11E+12	7.53E+11
Cell 6	01	01	140	195	2.11E+12	2.94E+12
Cell 7	01	10	140	330	2.11E+12	4.97E+12
Cell 8	01	11	140	500	2.11E+12	7.53E+12
Cell 9	10	00	260	50	3.91E+12	7.53E+11
Cell 10	10	01	260	195	3.91E+12	2.94E+12
Cell 11	10	10	260	330	3.91E+12	4.97E+12
Cell 12	10	11	260	500	3.91E+12	7.53E+12
Cell 13	11	00	450	50	6.77E+12	7.53E+11
Cell 14	11	01	450	195	6.77E+12	2.94E+12
Cell 15	11	10	450	330	6.77E+12	4.97E+12
Cell 16	11	11	450	500	6.77E+12	7.53E+12

5.4.1.2 Theoretical Evaluation

To estimate the theoretical limits on the maximum achievable ΔI_R enabled by an ERQ network (Figure 5-7a), we analyzed the steady-state response of ERQ-PEPE's under ideal photon arrival conditions where addressing photons (λ_Q) arrive before their

corresponding excitation photons (λ_E), e.g., two time-separated pulses. According to this analysis (see the Supporting Information) the maximum achievable ΔI_R by an ERQ network (PEPE) is given by the following formula in which k, τ and Φ are the transfer rate, intrinsic fluorescence lifetime and quantum yield, respectively. Further, I_E is the average number of photons absorbed per unit time by the E population.

$$\Delta I_R = I_E \Phi_R \frac{k_{ER}}{k_{ER} + 1/\tau_E} \left(1 - \frac{1}{1 + \frac{k_{EQ}}{k_{ER} + 1/\tau_E}} \times \frac{1}{1 + \tau_R . k_{RQ}} \right)$$

Evaluating the above formula using the specifications of the PEPE's that we synthesized (τ_E=3.56ns, τ_R=4.2ns, etc.) yields a maximum expected ΔI_R of ~52% with pulsed sources. With continuous (non-pulsed) light sources the photon arrival times are random and consequently the maximum expected ΔI_R reduces significantly (to ~1.7%) due mainly to two parasitic effects: 1- Self-Addressing, and 2-Belated-Addressing which are discussed in detail in the next sub sections.

5.4.1.2.1 Steady-state Approximation of ΔI_R

Under steady-state conditions (and no photo-bleaching) we can assume that the size of the excited-E population (i.e., [E*]) remains almost unchanged over time even though different E molecules might undergo excitation. Therefore the population of PEPE's can be thought of as a network with an influx of excitons (absorbed photons) to node E, a fraction of which is transferred to node R and eventually fluoresce out of the network. In the following paragraphs we have approximated the average fluorescence

intensity of R ($\mathfrak{F}_R$) before and after ERQ is addressed ($\mathcal{L}$ and $\mathcal{H}$ levels respectively). The difference between $\mathcal{H}$ and $\mathcal{L}$ yields ΔI_R under ideal timing conditions:

$$\Delta I_R = \mathcal{H} - \mathcal{L} = I_E \Phi_R \frac{k_{ER}}{k_{ER} + 1/\tau_E} \left(1 - \frac{1}{1 + \frac{k_{EQ}}{k_{ER} + 1/\tau_E}} \times \frac{1}{1 + \tau_R . k_{RQ}} \right)$$

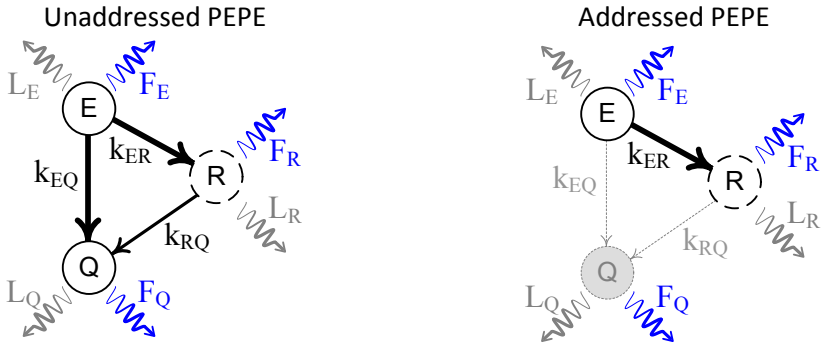

Figure 5-12: Relaxation pathways in a PEPE before and after full saturation

A) Unaddressed PEPE

The average number of photons per unit time fluoresced from R, is denoted by $\mathfrak{F}_R$ and depends on the rate of incoming excitons from E and the rate of fluorescence in presence of the quenching pathway from R to Q; therefore it can be written as:

$$\mathfrak{F}_R = excitons_{from\ E} \times efficiency_{fluorescence} = I_E \times \varphi_{ER} \times \varphi_{Fluor(R)}$$

In this formula φ_{ER} is the transfer efficiency of E to R, and $\varphi_{Fluor(R)}$ is the fluorescence efficiency (quantum yield) of R.

$$\varphi_{ER} = \frac{\text{transfer rate from E to R}}{\sum \text{relaxation rates of E}} = \frac{k_{ER}}{F_E + L_E + k_{ER} + k_{EQ}}$$

$$\varphi_{Fluor(R)} = \frac{\text{fluorescence rate of R}}{\sum \text{relaxation rates of R}} = \frac{F_R}{F_R + L_R + k_{RQ}}$$

Therefore $\mathfrak{F}_R$ can be expressed in terms of de-excitation rates as follows:

$$\mathfrak{F}_R = I_E \times \varphi_{ER} \times \varphi_{Fluor(R)} = I_E \times \frac{k_{ER}}{F_E + L_E + k_{ER} + k_{EQ}} \times \frac{F_R}{F_R + L_R + k_{RQ}}$$

Here, F_E and L_E denote the florescence- and loss rate of E respectively and I_E is the average number of photons per unit time absorbed by E. Since by definition, the intrinsic lifetime of E is $\tau_E = (F_E + L_E)^{-1}$ and the quantum yield of R is $\Phi_R = F_R/(F_R + L_R)$, we can further simplify the expression as follows, :

$$\boxed{\mathcal{L} = \mathfrak{F}_R = I_E \times \frac{k_{ER}}{\frac{1}{\tau_E} + k_{ER} + k_{EQ}} \times \frac{\Phi_R}{1 + \tau_R . k_{RQ}}}$$

In which $\mathcal{L}$ is the steady-state fluorescence intensity of R with unaddressed PEPE's under ideal timing conditions.

B) Addressed PEPE

In an addressed ERQ-PEPE, Q is occupied (excited) and therefore the two de-excitation pathways E→Q and R→Q are disabled, i.e., $k_{EQ} = k_{RQ} = 0$.

$$\mathfrak{F}_R = excitons_{from\ E} \times efficiency_{fluorescence}$$

$$\mathfrak{F}_R = I_E \times \varphi_{ER} \times \varphi_{Fluor(R)}$$

Since here $k_{EQ} = k_{RQ} = 0$, we have:

$$\mathfrak{F}_R = I_E \times \frac{k_{ER}}{k_{ER} + F_E + L_E} \times \frac{F_R}{F_R + L_R}$$

$$\boxed{\mathcal{H} = \mathfrak{F}_R = I_E \times \frac{k_{ER}}{k_{ER} + \frac{1}{\tau_E}} \times \Phi_R}$$

In which $\mathcal{H}$ is the steady-state fluorescence intensity of R with addressed PEPE's under ideal timing conditions.

5.4.1.2.2 Deterioration of ΔI_R

The calculations in the previous section are under ideal photon ordering (λ_Q arrives before λ_E); however, with random photon-arrival times, there is no control over the arrival ordering and consequently ΔI_R deteriorates mainly due to two parasitic effects: 1- Self-addressing, and 2- Belated-addressing which are explained using $\widehat{\Delta I_R}$, $\hat{\mathcal{H}}$ and $\hat{\mathcal{L}}$ to respectively refer to ΔI_R, $\mathcal{H}$ and $\mathcal{L}$ under continuous (non-pulsed) irradiation.

Self-addressing happens when in an unaddressed PEPE, the exciton at E reaches Q and while Q is still excited, another photon is absorbed by E. The unavailability of Q for quenching E creates a virtually addressed PEPE which parasitically increases the $\hat{\mathcal{L}}$ level and thereby deteriorating the observable ΔI_R.

In a PEPE with unexcited E, R and Q, belated-addressing occurs when in a read cycle, E is excited while Q is still unexcited (λ_E absorbed first, which is out of order) which creates an effectively unaddressed PEPE reducing the $\hat{\mathcal{H}}$ level and consequently diminishing $\widehat{\Delta I_R}$. (In a timely-addressed read cycle Q must be excited before E is excited).

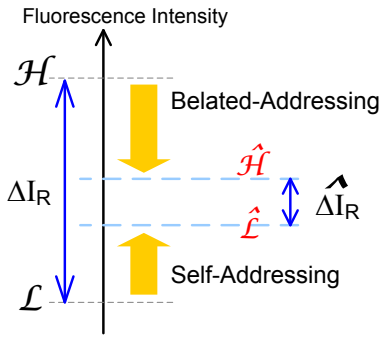

Figure 5-13: Deterioration of ΔI_R due to self-addressing and belated addressing

The deterioration of ΔI_R depends on the fraction of the PEPE population that is affected by these two effects. If fraction s of the PEPE population undergoes self-addressing the $\hat{\mathcal{L}}$ level increases by $s\mathcal{H}$ hence $\hat{\mathcal{L}} = [(1-s)\mathcal{L} + s\mathcal{H}]$. Similarly, when fraction b of the population undergoes belated-addressing the $\hat{\mathcal{H}}$ level decreases by $b\mathcal{L}$ and therefore $\hat{\mathcal{H}} = (1-b)\mathcal{H} + b\mathcal{L}$.

$$\widehat{\Delta I_R} = \hat{\mathcal{H}} - \hat{\mathcal{L}} = [(1-b)\mathcal{H} + b\mathcal{L}] - [(1-s)\mathcal{L} + s\mathcal{H}] = (1-b-s)\mathcal{H} - (1-s-b)\mathcal{L}$$

$$\gamma = 1-b-s \Rightarrow \boxed{\widehat{\Delta I_R} = \gamma(\mathcal{H}-\mathcal{L}) = \gamma.\Delta I_R}$$

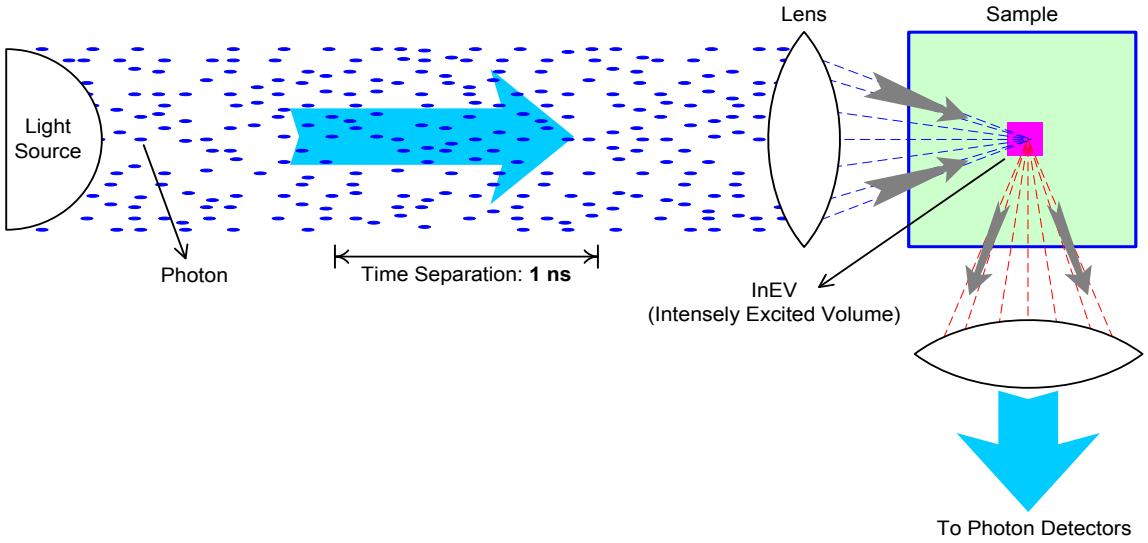

Figure 5-14: Excitation setup with focused beams – Formation of InEV enables achieving higher levels of saturation

In the above formula γ is the timing efficiency which varies between 0 and 1 depending on the relative arrival times of excitation and addressing photons. By reducing the inter arrival time of λ_Q photons we can reduce b and thereby partially improve γ because in this case λ_Q photons arrive more frequently and therefore fewer λ_E photons will be late relative to λ_Q photons. This partial improvement of γ can be

achieved with focused incident beams (Figure 5-14), by adjusting the intensity of the λ_Q beam such that it is relatively higher than that of the λ_E beam, as increasing the intensity of a focused beam reduces the effective inter arrival time of photons at the InEV. Even with tuned intensities, self-addressing is still a problem which can be resolved by using pulsed sources.

In our experiments $\widehat{\Delta I_R}$ was measured to be ~1.75% and by plugging the parameter values (extracted from PEPE specifications) into the above formula, ΔI_R is found to be ~52% which yields γ=0.033 for our experiments (assuming perfect photon detection).

5.4.2 Polychromatic Channels

5.4.2.1 Effect of inter-channel crosstalk (ICC) on channel capacity

Channel capacities are limited by inter-channel crosstalk (ICC) which is the parasitic (unwanted) activation of a channel when another channel is addressed. Ideally all address tags must be such spectrally distinct that exciting one cannot excite any other; in practice however, there might be some overlap in the excitation spectra of the tags, which results in crosstalk between address lines meaning that the excitation of one address tag, also partially excites another tag. Increase in tag crosstalk reduces the number of possible channels per cell and also lowers channel capacity (Y) as expressed in the following formula (c is the inter-channel crosstalk):

$$Y = \log_2\left(\frac{Signal}{c.Signal + Noise}\right) \xrightarrow{Noise \approx 0} Y = \lim_{\varepsilon \to 0} \log_2\left(\frac{\Delta I_{R_{max}}}{c \cdot \Delta I_{R_{max}} + \varepsilon}\right) = \log_2\left(\frac{1}{c}\right)$$

This formula originates from the fact that with a very low c, we can have a large number of distinguishable levels and thereby a high-capacity channel. For a set of channels with a fixed capacity, this formula sets an upper bound, shown in

Figure 5-15, on the maximum tolerable inter-channel crosstalk (ICC).

Figure 5-15 also reflects how much channel capacity is lost due to increase in ICC; specifically it shows that the ICC in any set of channels must be 50% or less, otherwise the entire channel capacities are lost and no data can be stored in any channel. This means that no data can be stored in, and reliably retrieved from, a set of channels with a maximum ICC of greater than 50%.

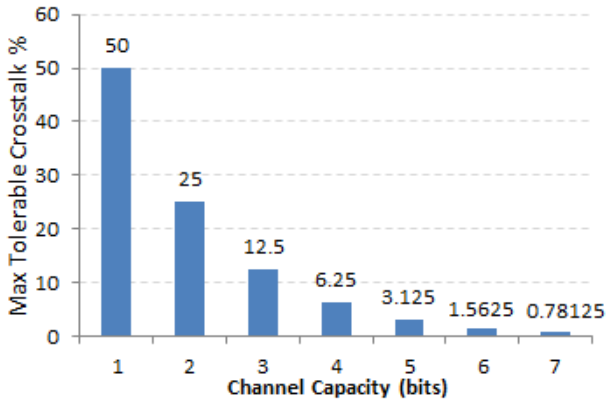

Figure 5-15: Maximum Tolerable Inter-channel Crosstalk (ICC). Even with single-bit channels, the maximum ICC cannot exceed 50%.

5.4.2.2 Simulation Results

To study storage cells with four channels we conducted a design search for quadruples of *commercially available* dyes to form ERQ²-PEPEs, i.e., (E, R, Q1, and Q2); however, since commercial dyes are not optimized for use in PAM, their spectral

properties violate the 50%-ICC requirement; specifically we were unable to find any pair of quadruples with an ICC of 50% or less. This present-day limitation on building multi-tag PEPEs (storage elements with multiple acceptors in their address vector) based on commercial dyes, is due to the lack of an exclusive excitation band in the excitation spectrum of these dyes to enforce a sufficiently-low ICC. Given these limitations we chose to *simulate* the response of multi-tag PEPEs, based on photophysically-plausible [36-38] synthetic spectra optimized for PAM, to estimate the theoretical limits on the capacity of PAM channels.

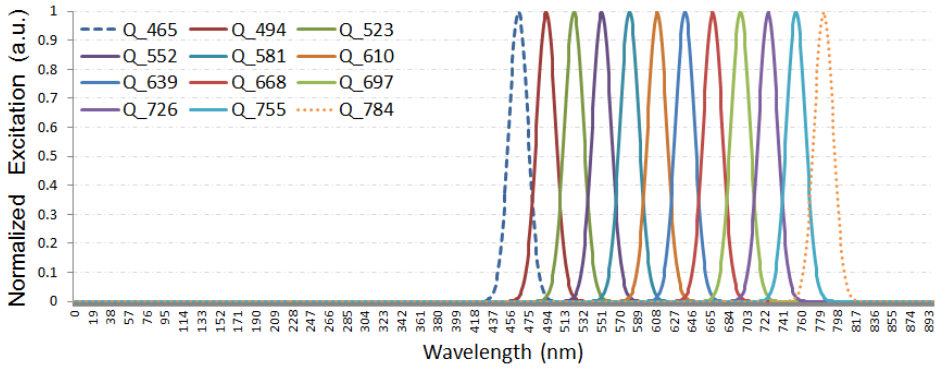

Figure 5-16 – Synthetic excitation spectra used in the simulations

We used a custom Monte-Carlo simulator based on [20], [18] and [24] to simulate all 924 possible distinct 6-color channels (Figure 5-17) out of a 12-color spectra-set (Figure 5-16) which we generated based on the average full-width at half-maximum (FWHM) of a representative set of commercially available fluorophores, and which we repeatedly shifted in wavelength by ~30nm to minimize ICC. The PEPEs were modeled such that the transfer efficiency from the excitation-port fluorophore to each address

port was at least 95%, which is feasible given the small separations permitted by attachment to the DNA scaffold and the number of available nucleotides for functionalization. Simulation results (see the Supporting Information) show that the $\Delta I_{R\text{-}max}$ for the ERQ^{6}-PEPEs ranges between 54% and 65%, which enables channel capacities of at least six bits per each channel yielding a total cell capacity of ~5500 bits (924x6), versus one bit for a DVD pit.

5.4.2.2.1 Storage Density Calculation

Storage elements are realized on DNA scaffolds each of which has a square shape with 20 nm by 20 nm sides and the thickness of the scaffold is ~2nm. To find the maximum theoretical density we calculated the number of scaffolds that can be packed in a volume such that they do not have functional interference (i.e. farther than Förster radius). The only way that two scaffolds may have functional interference is when they are vertically placed too close to one another. Therefore we assumed that a construct is a cubic volume with 20 nm sides. Because compared to the largest Förster radius, a vertical separation of 20 nm is far enough for the storage elements not to functionally interfere. The details of calculations are presented in the following tables.

Cell dimensions	
Base width	0.6 microns (chosen to be 0.6)
Base length	0.6 microns (chosen to be 0.6)
Height	1.397 microns (chosen to be 1.397)

Number of PEPE's (storage elements)		
Per cell base area	900 elements	$(0.6um)^2/(20nm)^2 = 900$
Per cell volume	62,865 elements	$1.397umx(0.6um)^2/(20nm)^3 = 62865$

Data Density		
Property	*Value*	*Calculation*
Bits per channel	6 bits	Chosen to be 6 bits per channel
Required PEPE's per channel	68 PEPE's	(2^(bits per channel)-1 = 2^6-1 = 63) + 8% redundancy
Channels per cell	924	(# PEPE)/(#PEPE per channel) = 62865/68 = 924
Bits per cell	5,544	#channels x #bits per channel = 920 x 6 = 5544
Areal density	1.4 Tb/cm^2	# cells per cm^2 x # bits per cell = (10K^2/0.6^2)x5.5K = 1.4

5.5 Discussion

The merit of PAM is that it enables an exponential increase of the number of addressable channels with respect to the size of the PAM-palette, i.e., the set of all different dyes that can be used as an acceptor in the address vector. Specifically, the optimum width of the address vector with a palette size of n is $\frac{1}{2}n$, which yields a total of $\binom{n}{n/2}$ distinct addresses (Figure 5-17). This rapid growth rate enables high storage densities, beyond the diffraction limit, even at low cell densities with only a handful of engineered dyes.

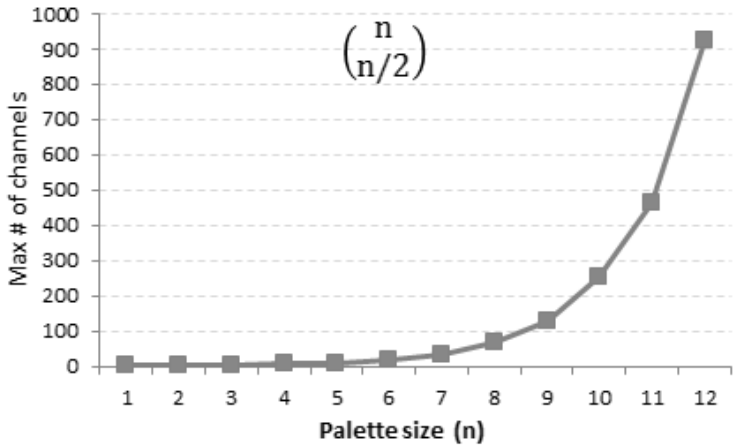

Figure 5-17: Number of addressable PAM channels exponentially grows with the pallet size (n); e.g. with n=12, a total of 924 channels can be addressed.

5.6 Summary and conclusion

In summary, we demonstrated a novel addressing technique called polychromatic address multiplexing (PAM) which, among its various applications, has the potential to enable several-thousand-fold increase in the areal storage density of optical discs beyond the diffraction limit. PAM exploits acceptor saturation in precisely-assembled nanoscale FRET-based structures to induce a fluorescence increase which is exclusively caused by the addressed structures while other structures remain inactive. Using commercially available dyes, we synthesized two kinds of storage elements to experimentally demonstrate, as a proof-of-concept, storage cell capacities of two, three and four bits. We also simulated 6-color storage-elements based on PAM-optimized synthetic dyes and the channel capacities were shown to be at least six bits. The exponential growth of the address space enabled by PAM makes it an efficient technique for many data-multiplexing applications including, but not limited to, optical storage media.

5.7 Experimental Section

The PEPEs were realized on self-assembled DNA tiles with fluorophores covalently bound to the 5′ or 3′ end of DNA strands by a maleimide-thiol reaction the yields of which were verified by capillary gel electrophoresis. The DNA tile structure was used to hold the three fluorophores at specific positions to enforce the intended FRET network of Figure 5-7a. Each DNA tile was composed of nine single-stranded

DNA chains the sequences of which were designed such that after hybridization, the cruciform of Figure 5-7b was formed (see the Supporting Information). The strand mixture was annealed by heating to 96°C followed by cooling to 4°C over 4 h and incubation at 4°C for 12h.

All measurements were performed in 50uL cuvettes with PEPEs in Tris-acetate, EDTA buffer (TAE) and Mg-acetate (12.5 mM) at pH 7.5 and room temperature. Measurements of ΔI_R were made using a commodity CCD-based spectrometer (USB2000 OceanOptics, Inc.) for ERQ_{647} and ERQ_{TR} and they reliably showed 1.75% and 1.80% fluorescence increase upon address excitation, respectively, with 0.1% RMS detector noise.

6 Time-resolved Address Multiplexing (TAM)

The address range of polychromatic address multiplexing (PAM) depends on the palette size that is used for addressing, and also the quality of the palette which in turn depends on the spectral properties of its dye molecules. With a small or a low-quality (with high crosstalk) palette, PAM cannot provide high density. Yet it is possible to employ a sequential addressing scheme that uses a small set of fluorophores (instead of a large palette) and covers a wide addressing range. The main goal in time-resolved address multiplexing (TAM) is to expand the address range with minimal use of new fluorophore types.

6.1 Symbols and Addresses

An address in TAM is a sequence of possibly repeated symbols with different arrival times; this implies that TAM is a serial addressing scheme which does not apply all the symbols in parallel. A symbol itself is composed of a set of well-timed pulses of different wavelengths. We use the term "addressing alphabet" to refer to the set of all symbols used for addressing. The alphabet in TAM is equivalent to the palette in PAM with the difference that the former uses fewer distinct wavelengths than the latter.

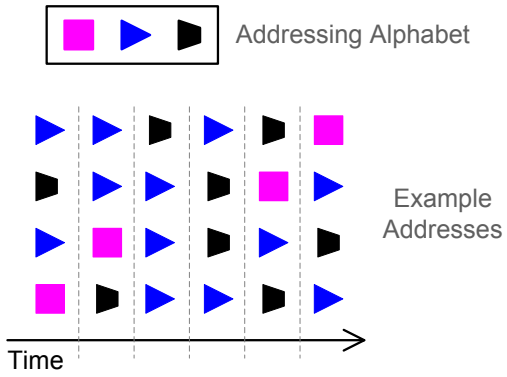

Figure 6-1 – A small alphabet yields a large address space; in this example 729 addresses are covered by the given alphabet (36)

Figure 6-1 shows some examples of the addresses that can be used in TAM. As seen in the figure, with a six-letter address and only three symbols we can cover an address space with 729 distinct addresses.

6.2 Storage Element

A TAM-compatible storage element is similar to a PEPE with the difference that it is activated by an address decoding network which can detect sequences of symbols that are serially applied to it (Figure 6-2). The address decoding network is typically

larger than the quenching network used in a PAM-storage element (augmented PEPE). The write process is still the same, i.e. the R flurorophore is detached from the storage element when it is written to.

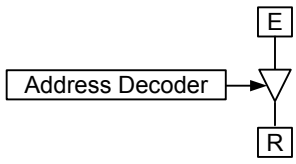

Figure 6-2 – Logical equivalent of the storage element used in TAM

As shown in Figure 6-3 a storage cell contains a large number of these storage elements with different addresses. Upon reading the contents of a channel only those storage elements contribute to the read-signal that have received a matching address.

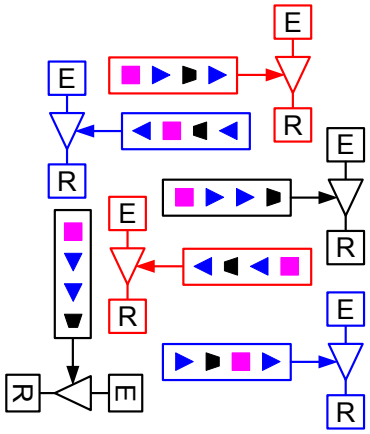

Figure 6-3 – Each cell is packed with storage elements with different address tags. – Only do those storage elements contribute to the R-signal, that have the matching symbol-sequence (address).

6.3 How TAM Works

Before reading a channel in TAM, a sequence of symbols (i.e. the address) is serially applied to the cell. All the storage elements in the cell receive the symbols and start

decoding them. After each symbol a special pulse, called the clock pulse, is also applied to the cell which is used by the decoders for synchronization purposes. Once the address is fully applied to the cell, the corresponding channel is activated and at this time the E pulse is applied and subsequently the R signal is collected which will give us the value of the channel.

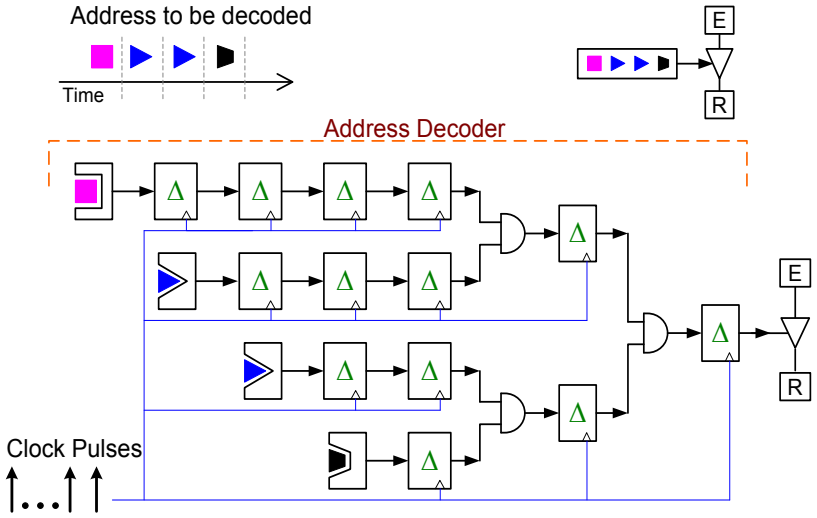

Figure 6-4 – Overview of TAM operation: the decoder network has a number of chains, each of which starts with a symbol detector. Once the detector receives the right symbol, it creates a charge (exciton charge) on its output which is carried to the end of the chain by clock pulses. At the end of the chains, all synchronized charges are ANDed together to enable signal propagation from the E to the R port.

The decoder is responsible for matching its address with the given address. It is composed of repeater chains that start with symbol detectors and end at an AND gate. As mentioned before, each symbol is a sequence of well-timed pulses and a symbol detector is a special FRET network that is activated only by a particular symbol. A repeater is sensitive to clock pulses and acts like a D flip-flop.

The architecture of a decoder is depicted in Figure 6-4. The symbols are applied between two consecutive clock pulses. As seen in the figure for example when the square symbol arrives the response of the detector is sent through four repeaters because three more symbols have to be also applied before we can AND them. The repeaters also perform signal restoration and therefore we can have arbitrarily long chains of repeaters.

6.3.1 Symbol Detectors

An excited population of fluorophores does not immediately de-excite and therefore can be treated as a temporary and short lived memory. This forms the basis of symbol detection. A symbol detector is expected to generate an excited population upon the reception of the right symbol (sequence of pulses).

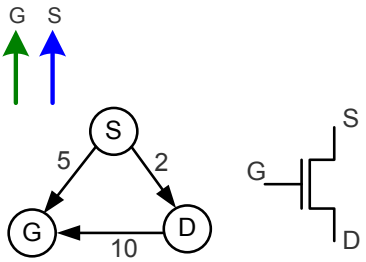

Figure 6-5 – A symbol detection network that detects symbols with two pulses of different wavelengths – if the green pulse is applied to G first and then after a short while the blue pulse is applied to S, most of the energy goes to D since G is not available enough to depopulate S and D

The RET network of Figure 6-5 can detect symbols which have only two pulses. The transfer rates in this network are important; specifically the D→G link has to be highly efficient as well as the S→G link. The S fluorophore is normally depopulated (quickly) by the G fluorophore which also depopulates the D fluorophore. Hence when

G is fully available populating S weakly populates D because of G. However, when G is prepopulated it is not available for depopulating A and D and therefore this time, populating S populates D too (green curve). Figure 6-6 shows the simulation of such a detector with and without prepopulated G.

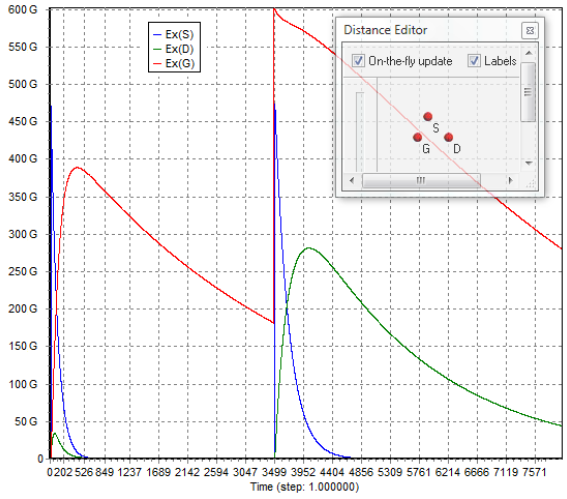

Figure 6-6 – Simulation of a symbol detector with and without G being prepopulated

The choice of S, G and D fluorophores depends on what wavelengths we want to detect and also how separated they are. In the example of Figure 6-6 which detects a symbol with the 405nm and 600nm wavelengths, AF 405, AF 546 and AF 594 are used as S, D and G respectively.

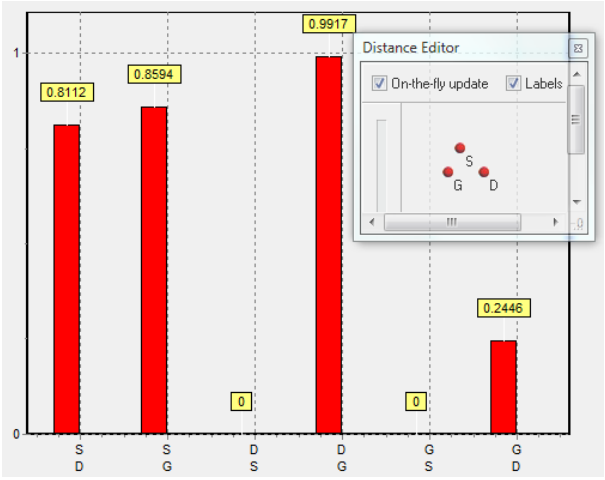

Figure 6-7 – Transfer efficiencies in the simulated symbol detector: The D→G link has to be highly efficient.

As shown in Figure 6-7, among the transfer efficiencies in this detector, the D→G link has the highest transfer efficiency.

6.4 TAM versus PAM

The exponential growth of address range exists in both TAM and PAM: the former with respect to the alphabet size and the latter with respect to the palette size. However TAM has several advantages over PAM. First of all, it is easier in TAM to have wider addresses (with more letters) because in PAM we are geometrically restricted whereas this restriction does not exist in TAM. The second advantage of TAM is its less sensitivity to crosstalk. Since with each clock pulse all the signals are restored back to their proper levels, inter channel crosstalk does not increase with the wider addresses in TAM whereas in PAM it does.

Overall TAM can effectively cover a larger address space (at the cost of linearly growing access time) since it is less restricted by various parameters such spectral properties of the dyes, geometry of storage elements, etc.

7 Future Work

The work in this thesis gives rise to new challenges and questions which are worth being investigated as separate research topics. Here, we briefly describe two of these research directions.

The PAM technique clearly highlights the need for dyes with narrow excitation bands. Specifically, one of the major limiting factors in PAM is the channel crosstalk which is caused by parasitic excitation of a fluorophore when other fluorophores are being addressed. The easiest solution to this problem is to use dyes that are excited only by a very narrow range of wavelengths. Despite being possible, in principle, such dyes are not commercially available at present. Therefore, research on PAM-compatible dyes is one of the possible future directions.

Another research direction is photo-induced RET modulation (piRET) which is useful in implementing more efficient switching functionality in FRET circuits. Specifically, the switching functionality in FRET circuits is currently achieved through acceptor saturation wherein the acceptor of a RET path is continuously kept excited, and thereby that RET path is (partially) blocked. This technique has the drawback of requiring high photon densities which are practically hard to achieve without a special focusing setup, which in turn, has undesired side effects. One of the alternatives to acceptor saturation is photo-induced RET modulation (piRET), due to which the transfer efficiency of a RET pair is (preferably highly) influenced by the presence of a particular

wavelength of light. For example, one could imagine a donor-acceptor pair which is normally weak, but in the presence of violate light becomes very strong. Using piRET enables FRET circuits to operate at low concentrations without the need for focusing instruments.

Appendix A – Detailed Flowchart of Karoon

As illustrated in Figure A0-1, Karoon starts with the initialization step in which the required data structures are created and initialized, in particular, to represent the population profile an array is created each entry of which is uniquely associated with the size of a particular stratum, and stores the most recent size of that stratum throughout the simulation. Initially, (i.e., at time t=0), all the entries of this array, except the first one, are set to zero, as all the fluorophores are assumed to be initially unexcited. Thus, the first entry of the array, which corresponds to the case of all-unexcited fluorophores, is initialized with the total number of multi-fluorophore structures in the sample. In addition to the population profile, an array of counters is allocated for each excitation or de-excitation pathway; for example, one array per node is allocated to keep track of the number of fluoresced photons out of the corresponding node during each time slice. Similarly, separate event counters per node are allocated for exciton loss and every pairwise RET path, as well as for external excitation sources (such as absorbed photons).

The length of these event counters, all of which are initialized with zero, equals the number of time slices. Furthermore, over the course of simulation, each stratum independently contributes to these event counters.

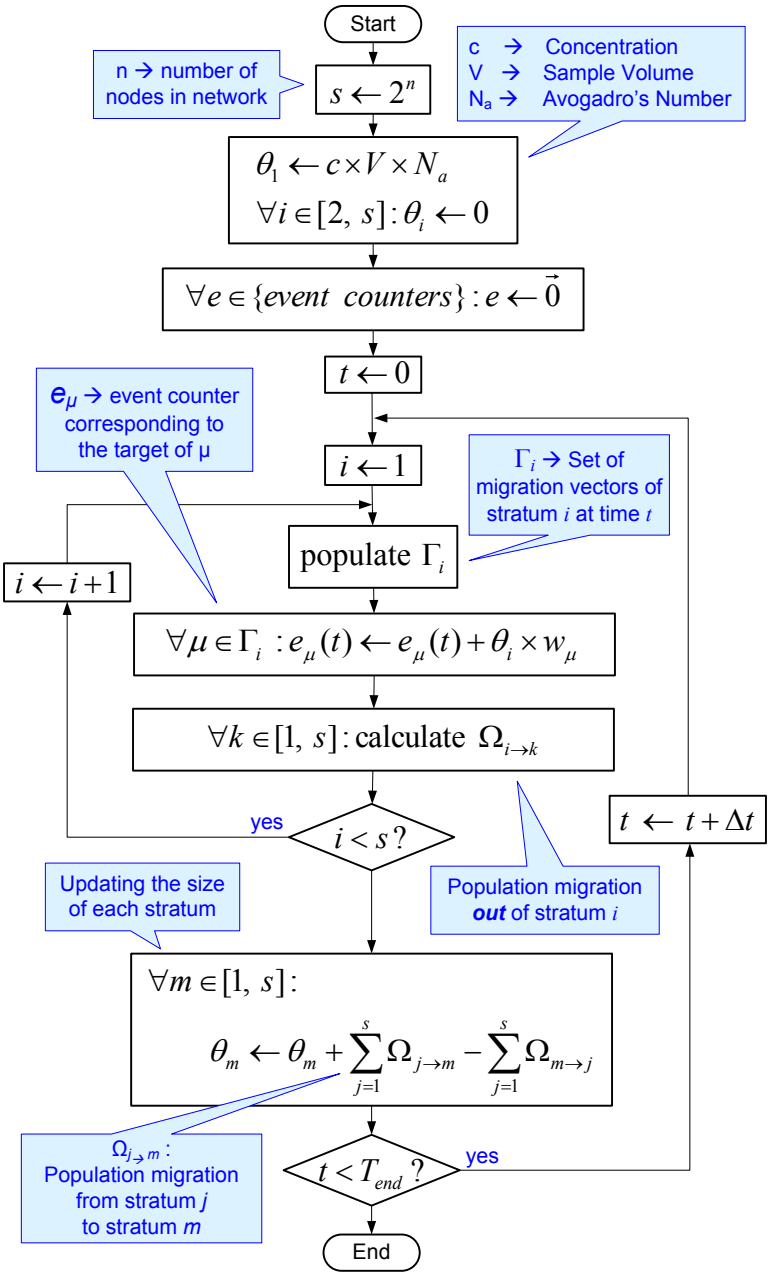

Figure A0-1 – Detailed flowchart of Karoon

After the initialization step, Karoon iteratively simulates the exciton flow in the given RET network. In each iteration (time step), every stratum is independently processed to determine its contribution to the corresponding event counters. These

contributions are proportional to the size (θ_i) of the contributing stratum which is stored in the population profile. For instance, the total RET from D to A during time slice t is obtained from Eq.8 in which s is the number of strata in the population profile and $w_{R(i,D\to A)}$ denotes the RET weight of the D→A pair in stratum i. As deduced from this equation, if a stratum is not sufficiently populated at time t (e.g., $\theta_i(t) \approx 0$) it does not noticeably contribute to the total RET. Likewise, the total number of fluoresced photons out of node D during time slice t, denoted by $\mathfrak{F}(D,t)$, is given by Eq.6 wherein E(D) is the set of strata in which D is excited.

Migration weights (w_F, w_R, etc.) are calculated at the beginning of each time slice. Unlike *effective* RET-rate constants, which vary over the course of simulation, migration weights are constant and thus can be alternatively pre-calculated in the initialization step and stored in memory to be used in the rest of the simulation.

During every time slice, some fraction of the population of each node changes in excitation state and consequently the size of each stratum changes. Thus, at the end of each time slice, the population profile is updated to be used in the next time slice, and the simulation time is advanced by Δt.

A c++ implementation of Karoon is available to download as part of a toolkit called *RETCAD* at **www.retcad.com**. Among many other tools, this toolkit has a simulation environment which supports several simulation algorithms including Karoon and the classical method (i.e., ode).

Appendix B – Calculation of inter-stratum population migration (ISPM)

In order to keep the population profile up-to-date, in each time step, the emigrating population out of each stratum to all other strata is calculated. Every de-excitation or excitation process (e.g., light absorption, RET, fluorescence, etc.) is represented by a migration vector (which has a weight and a target). As explained in the following example, these vectors split the stratum population into a number of slices, each of which corresponds to a target stratum. Upon the application of every vector, its weight is proportionally distributed across the affected existing slices, and thereby new slices are created.

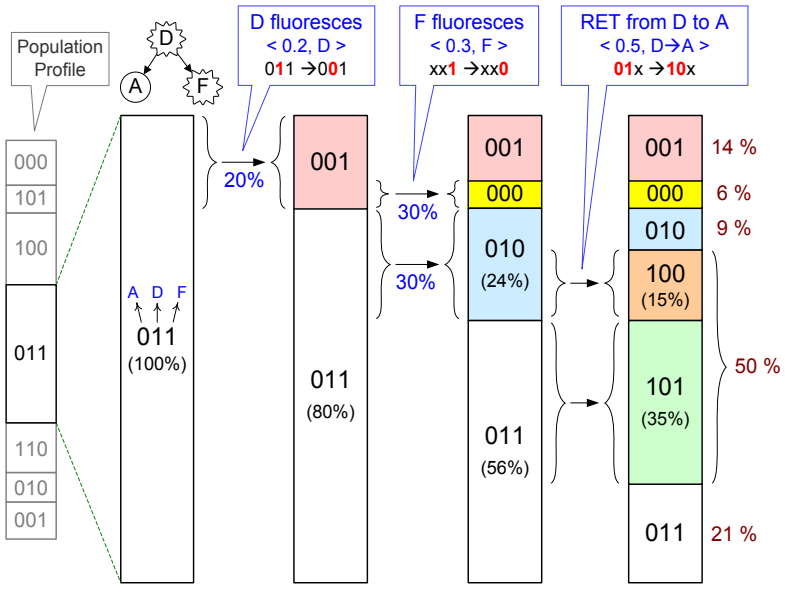

Figure A0-2. Stratum slicing for stratum *011* – At the end of each time step, 21% of the 011-population remains in this stratum and the rest migrate to 5 other strata {14% to 001, 6% to 000 … }

In the network of Figure A0-2, D is a common donor to A and F (A←D→F). In stratum 011, two migration vectors are inactive: first, the D→F path, since D and F are both excited, and second, A's fluorescence, because A is not excited in this stratum. Therefore, ignoring exciton loss, only three migration vectors apply to stratum 011, which are fluorescence of D and F, and RET from D to A, denoted by <0.2, D>, <0.3, F>, and <0.5, D→A>, respectively (in Figure A0-2). Table A0-1 summarizes a step-by-step calculation of ISPM for stratum 011.

Table A0-1 – Step-by-step example of stratum-population slicing

<table>
<tr><th>Step</th><th>Slices</th><th>Description</th></tr>
<tr><td>1</td><td>{011}</td><td>Initially there is only one slice which contains 100% of the 011-population.</td></tr>
<tr><td>2</td><td>{011}
New:{010}</td><td>One vector is applied (say <0.2, D>) and divides the population into two slices:
20% undergoes fluorescence (of D) and changes from 011 to 001, and 80% remains unchanged (i.e., 001)</td></tr>
<tr><td>3</td><td>Existing:
{011,001}

Newly created:
{010,000}</td><td>The next vector is the fluorescence of F (i.e., <0.3, F>); therefore, it applies only to those slices in which F is excited.
30% of each target slice undergoes fluorescence (of F). Since both of the existing slices (i.e., 001 and 011), are affected by this vector, two new slices, namely 000 and 010 are formed which are 6% and 24% in size (see table below).
<table>
<tr><th>Existing Slices (old excitation status)</th><th>Current Size</th><th>Affected Size</th><th>New Excitation (Affected) Status</th></tr>
<tr><td rowspan="2">001</td><td rowspan="2">20%</td><td>20/(20+80)% x 30% = 6%</td><td>000</td></tr>
<tr><td>20% - 6% = 14%</td><td>001 (unchanged)</td></tr>
<tr><td rowspan="2">011</td><td rowspan="2">80%</td><td>80/(20+80)% x 30% = 24%</td><td>010</td></tr>
<tr><td>80% – 24% = 56%</td><td>011 (unchanged)</td></tr>
</table></td></tr>
<tr><td>4</td><td>Existing:
{011,010, 001,000}

Newly created:
{100, 101}</td><td>The last vector is the RET path from D to A (i.e., <0.5, D→A>), therefore it only applies to those slices in which D is excited and A is not.
Only two of the four slices can undergo RET (D→A). The vector's weight (i.e., 50%) is proportionally divided between these two slices (35% for 011, and 15% for 010).
<table>
<tr><th>Existing Slices (old excitation status)</th><th>Current size</th><th>Affected Size</th><th>New Excitation (Affected) Status</th></tr>
<tr><td>001</td><td>14%</td><td>Not affected</td><td>001 (14%)</td></tr>
<tr><td>000</td><td>6%</td><td>Not affected</td><td>000 (06%)</td></tr>
<tr><td rowspan="2">011</td><td rowspan="2">56%</td><td>56/(56+24)% x 50% = 35%</td><td>101 (35%)</td></tr>
<tr><td>56% – 35% = 21%</td><td>011 (21%)</td></tr>
<tr><td rowspan="2">010</td><td rowspan="2">24%</td><td>24/(56+24)% x 50% = 15%</td><td>100 (15%)</td></tr>
<tr><td>24% – 15% = 9%</td><td>010 (09%)</td></tr>
</table></td></tr>
</table>

References

1. Lakowicz, J.R., *Principles of Fluorescence Spectroscopy*1999, New York: Kluwer Academic / Plenum Publishers.

2. Pistol, C., et al., *Encoded multi-chromophore response for simulataneous label-free detection.* Small, 2010. **6**(7): p. 843-850.

3. Beutler, M., et al., *Satfret: Estimation of F*rster Resonance Energy Transfer by Acceptor Saturation.* European Biophysics Journal, 2008. **38**: p. 69--82.

4. Valeur, B., *Molecular Fluorescence: Principles and Applications*2002, Weinheim: Wiley-VCH.

5. Hoppe, A.D., et al., *N-way FRET microscopy of multiple protein-protein interactions in live cells.* PLoS ONE, 2013. **8**(6): p. e64760.

6. Sekar, R.B. and A. Periasamy, *Fluorescence resonance energy transfer (FRET) microscopy imaging of live cell protein localizations.* J Cell Biol, 2003. **160**(5): p. 629-33.

7. Freeman, R., et al., *Biosensing and probing of intracellular metabolic pathways by NADH-sensitive quantum dots.* Angew Chem Int Ed Engl, 2009. **48**(2): p. 309-13.

8. Sohn, H.W., et al., *Fluorescence resonance energy transfer in living cells reveals dynamic membrane changes in the initiation of B cell signaling.* Proc Natl Acad Sci U S A, 2006. **103**(21): p. 8143-8.

9. Medintz, I.L., et al., *Self-assembled Nanoscale Biosensors Based on Quantum Dot FRET Donors.* Nature Materials, 2003. **2**(9): p. 630-638.

10. Pistol, C., et al., *Encoded multichromophore response for simultaneous label-free detection.* Small, 2010. **6**(7): p. 843-50.

11. Trang, T.T., et al., *Enhanced light harvesting from Forst-type resonance energy transfer in the quasi-solid state dye-sensitized solar cells.* J Nanosci Nanotechnol, 2012. **12**(4): p. 3301-4.

12. Pistol, C., et al., *Architectural Implications of Nanoscale-Integrated Sensing and Computing.* Micro, IEEE, 2010. **30**(1): p. 110-120.

13. Firdaus, K., T. Nakamura, and S. Adachi, *Improved lasing characteristics of ZnO/organic-dye random laser.* Applied Physics Letters, 2012. **100**(17).

14. Mottaghi, M.D. and C. Dwyer, *Thousand-fold increase in optical storage density by polychromatic address multiplexing on self-assembled DNA nanostructures.* Adv Mater, 2013. **25**(26): p. 3593-8.

15. Wolber, P.K. and B.S. Hudson, *An analytic solution to the Forster energy transfer problem in two dimensions.* Biophys J, 1979. **28**(2): p. 197-210.

16. Berney, C. and G. Danuser, *FRET or No FRET: A Quantitative Comparison.* Biophysical Journal, 2003. **84**: p. 3992-4010.

17. Demidov, A.A., *Use of Monte Carlo method in the problem of energy migration in molecular complexes*. Resonance Energy Transfer, ed. D.L. Andrews1999: Wiley. 488.

18. Frederix, P., et al., *Dynamic Monte Carlo Simulations to Model FRET and Photobleaching in Systems with Multiple Donor-acceptor Interactions.* Journal Of Physical Chemistry B, 2002. **106**(26): p. 6793-6801.

19. Berberan-Santos, M.N., et al., *Multichromophoric Cyclodextrins. 6. Investigation of Excitation Energy Hopping by Monte-Carlo Simulations and Time-Resolved Fluorescence Anisotropy.* Journal of the American Chemical Society, 1999. **121**(11): p. 2526-2533.

20. Corry, B., D. Jayatilaka, and P. Rigby, *A Flexible Approach to the Calculation of Resonance Energy Transfer Efficiency Between Multiple Donors and Acceptors in Complex Geometries.* Biophysical Journal, 2005. **89**(6): p. 3822-3836.

21. Dunn, W.L. and J.K. Shultis, *Exploring Monte Carlo methods.* Choice: Current Reviews for Academic Libraries, 2011. **49**(3): p. 548-548.

22. Förster, T., *Intermolecular energy migration and fluorescence.* Annals of Physics, 1948. **2**: p. 55.

23. Watrob, H.M., C.-P. Pan, and M.D. Barkley, *Two-Step FRET as a Structural Tool.* Journal of the American Chemical Society, 2003. **125**: p. 7336-7343.

24. Wolfgang, E., H. Ruediger, and D. Heinz, *Structure-based calculation of multi-donor multi-acceptor fluorescence resonance energy transfer in the 4*6-mer tarantula hemocyanin.* Eur Biophys J, 2004. **33**: p. 386-395.

25. Neifeld, M.A. and W.-C. Chou, *Information Theoretic Limits to the Capacity of Volume Holographic Optical Memory.* Appl. Opt., 1997. **36**(2): p. 514-517.

26. Lu, Z. and Y. Liu, *Rewritable multicolor fluorescent patterns for multistate memory devices with high data storage capacity.* Chem. Commun., 2011. **47**(34 The Royal Society of Chemistry): p. 9609-9611.

27. Li, J., et al., *Two-dimensional shift-orthogonal random-interleaving phase-code multiplexing for holographic data storage.* Optics Communications, 2011. **284**(24): p. 5562-5567.

28. Chon, J., et al., *Spectral Encoding on Gold Nanorods Doped in a Silica Sol*gel Matrix and Its Application to High-density Optical Data Storage.* Adv. Funct. Mater., 2007. **17**(6 WILEY-VCH Verlag): p. 875-880.

29. Corredor, C., et al., *Two-photon 3d Optical Data Storage Via Fluorescence Modulation of an Efficient Fluorene Dye by a Photochromic Diarylethene.* Adv. Mater., 2006. **18**(21 WILEY-VCH Verlag): p. 2910-2914.

30. Giordano, L., et al., *Diheteroarylethenes as Thermally Stable Photoswitchable Acceptors in Photochromic Fluorescence Resonance Energy Transfer (pcFRET).* J. Am. Chem. Soc., 2002. **124**(25): p. 7481-7489.

31. Tseng, S.-C., et al., *A permanent optical storage medium exhibiting ultrahigh contrast, superior stability, and a broad working wavelength regime.* Phys. Chem. Chem. Phys., 2011. **13**(13): p. 5747-5752.

32. Kryuchyn, A.A., V.V. Petrov, and S.O. Kostyukevych, *High density optical recording in thin chalcogenide films.* Journal of Optoelectronics and Advanced Materials, 2011. **13**(11-12): p. 1487-1492.

33. Olejnik, J., et al., *Photocleavable Aminotag Phosphoramidites for 5'-termini Dna/rna Labeling.* Nucleic Acids Res., 1998. **26**(15): p. 3572-6.

34. Hannestad, J.K., P. Sandin, and B. Albinsson, *Self-assembled DNA Photonic Wire for Long-range Energy Transfer.* Journal of the American Chemical Society, 2008. **130**(47): p. 15889-15895.

35. Pistol, C. and C. Dwyer, *Scalable, low-cost, hierarchical assembly of programmable DNA nanostructures.* Nanotechnology, 2007. **18**: p. 125305-9.

36. Hales, J.M., et al., *Design of Polymethine Dyes with Large Third-order Optical Nonlinearities and Loss Figures of Merit.* Science, 2010. **327**(5972): p. 1485-1488.

37. Matichak, J.D., et al., *Using End Groups to Tune the Linear and Nonlinear Optical Properties of Bis(dioxaborine)-Terminated Polymethine Dyes.* ChemPhysChem, 2010. **11**(1): p. 130-138.

38. Canton, G., et al., *Modified Stöber Synthesis of Highly Luminescent Dye-doped Silica Nanoparticles.* Journal of Nanoparticle Research, 2011. **13**(9): p. 4349-4356.

Biography

Mohammad Mottaghi Dastjerdi was born in Isfahan, Iran. He received his bachelor's degree in Computer Hardware engineering, and his master's degree in Computer-Systems Architecture. He started his Ph.D. at Duke University in January 2009, under the supervision of Dr. Christopher L. Dwyer, and worked on FRET-Enabled optical computing. He finished his Ph.D. in February 2014.